Structure and tectonics of the erosional convergent margin off Antofagasta, north Chile (23°30′S)

Valentí Sallarès[1]
UMR Géosciences Azur, Institut de Recherche pour le Développement, Villefranche-sur-Mer, France

César R. Ranero[2]
Das Leibniz-Institut für Meereswissenschaften an der Universität Kiel (IFM-GEOMAR) and SFB 574, Kiel, Germany

Received 2 September 2004; revised 9 December 2004; accepted 10 February 2005; published 10 June 2005.

[1] Subduction erosion has dominated the evolution of the north Chile convergent continental margin since at least the Mesozoic. We investigate the structure of the Antofagasta (23°S) sector of this margin along a transect using coincident wide-angle and near-vertical seismic profiling and gravity data. A 2-D velocity field of the overriding and subducting plates was obtained using joint refraction and reflection travel time tomography. A velocity-derived density distribution was used to model marine gravity data and substantiate the velocity model. The gravity and velocity models imply that the overriding plate is mainly made of arc-type igneous basement. The upper plate is constructed of two main rock bodies separated by a subhorizontal layer defined by a velocity inversion, the top coincident with a reflection in near-vertical seismic images. The seismic boundary is interpreted as a detachment separating an upper extended domain with large-scale normal faulting from a lower domain apparently undergoing a different type of deformation. Velocity-derived porosity indicates that the front of the margin is probably fluid-saturated and disaggregated by fracturation as a consequence of frontal subduction erosion. Fluids carried into the subduction channel within slope debris filling underthrusting grabens reduce basal friction and probably induce hydrofracturing and basal erosion along the underside of the overriding plate. At depths greater than ~20 km, porosity and density values imply that most fluids have been exhausted and the lower part of the upper plate is structurally coherent and little fractured. The change in physical properties leads to increased mechanical coupling along the plate boundary and occurs at the updip limit of the distribution of aftershocks of the 1995 Antofagasta earthquake (M_w = 8.0) defining the seismogenic zone.

Citation: Sallarès, V., and C. R. Ranero (2005), Structure and tectonics of the erosional convergent margin off Antofagasta, north Chile (23°30′S), *J. Geophys. Res.*, *110*, B06101, doi:10.1029/2004JB003418.

1. Introduction

[2] Subduction erosion dominates tectonics at least at 50% of all convergent margins [*von Huene and Scholl*, 1991]. Along the circum-Pacific subduction zones, long-term subduction erosion has been recognized in NE Japan and Peru [*von Huene and Lallemand*, 1990], north Chile [*Rutland*, 1971; *von Huene and Ranero*, 2003], along Pacific Middle America [*Ranero and von Huene*, 2000; *Ranero et al.*, 2000; *von Huene et al.*, 2000; *Vannucchi et al.*, 2003, 2004], Tonga [*Ballance et al.*, 1989; *Pelletier and Dupont*, 1990], and the Mariana trench [*Hussong and Uyeda*, 1981]. Tectonic erosion removes material from the overriding plate and inputs it into the subduction channel, the material is transported into the subducting zone and recycled into the mantle along with oceanic lithosphere. Material removal may occur by frontal erosion, when topographic features on the incoming oceanic plate collide with the apex of the margin and breach the slope toe, or by basal erosion, when material is removed along the underside of the upper plate. Subduction erosion thins the upper plate, leading to large-scale, long-term margin subsidence with steepening of the continental slope, to a progressive landward migration of the trench axis and to a similar migration of the volcanic arc. Despite the widespread occurrence of basal erosion, the mechanisms driving the process are poorly understood.

[3] The northern Chilean margin has been long recognized as dominated by subduction erosion [e.g., *Miller*,

[1]Now at Unitat de Tecnologia Marina, Centre Mediterrani d'Investigacions Marines i Ambientals, Consejo Superior de Investigaciones Científicas, Barcelona, Spain.

[2]Now at Institució Catalana de Recerca i Estudis Avançats, Institut de Ciències del Mar, Centre Mediterrani d'Investigacions Marines i Ambientals, Consejo Superior de Investigaciones Científicas, Barcelona, Spain.

0148-0227/05/2004JB003418$09.00

1970; *Rutland*, 1971; *Kulm et al.*, 1977; *von Huene and Lallemand*, 1990]. Tectonic erosion has been active here since the late Jurassic, as inferred from the progressive eastward migration of the volcanic arc during the past ~140 m.y. [e.g., *Rutland*, 1971]. The Jurassic arc crops out along the coastal areas and the location of the current arc indicates a total eastward migration of ~200 km.

[4] Along the north Chile trench, the ~48-m.y.-old Nazca plate subducts at ~100 km/m.y. beneath the South American plate, in a direction ~N75°E, roughly perpendicular to the regional trend of the margin [*Pardo Casas and Molnar*, 1987] (Figure 1). The plate is covered by less than 100 m of pelagic sediment and the trench is dominantly sediment starved. Since the Miocene, the arid climate of the Atacama desert along much of the north Chile forearc has produced little sediment and inland basins trap most of the scarce erosional products [*Hartley and Chong*, 2002]. Thus little continental sediment is supplied to the margin slope and trench [*Fisher and Raitt*, 1962; *Hayes*, 1966]. The bulk of the continental margin is constructed of Jurassic arc and older cratonic basement covered by a thin sequence of younger sediment. The incoming plate has a rough horst and graben topography exhibiting several hundred meters of relief on the outer trench slope and sediment-starved trench axis (Figure 1). However, subduction-erosion caused progressive steepening of the continental slope induces mass wasting of slope sediment that is delivered to the trench, filling the incoming grabens at the base of the slope. The infilling debris may be up to 1 km thick and is largely subducted, thus transporting a significant amount of fluids into the subduction zone [*von Huene and Ranero*, 2003].

[5] In northern Chile, the stress regime across the coastal region and continental slope is extensional [*Armijo and Thiele*, 1990; *Delouis et al.*, 1998; *von Huene and Ranero*, 2003]. The tectonic structure along a ~200-km-long segment of the margin was previously studied with multibeam bathymetry, a prestack depth migrated seismic reflection record across the slope, high-resolution seismic profiles in the continental shelf, and integration of onshore field studies [*von Huene and Ranero*, 2003]. The study of *von Huene and Ranero* [2003] documents a consistent tectonic structure along the ~200-km-long segment of the margin and proposes that the extension across the outer forearc, including coastal and slope areas, is primarily the result of gravitational destabilization of the margin framework caused by the steepening of the margin related to progressive subduction erosion.

[6] This paper uses the offshore and onshore recordings a wide-angle profile and coincident marine gravity data collected during *SONNE* 104 cruise [*Hinz et al.*, 1995] to obtain the velocity and density structure of the margin offshore Antofagasta (23.5°S) (Figure 1). The geophysical models are used to infer the nature of the margin rocks, their porosity and the fluid distribution. The distribution of physical properties has been integrated with the tectonic structure from coincident seismic reflection images to investigate how material properties and fluid distribution influence subduction erosion processes and the long-term tectonic evolution of the margin. Furthermore, changes in physical properties with depth are found to correlate with the transition along the plate boundary from aseismic creep to the stick-slip behavior of the seismogenic zone defined by the aftershocks of the 1995 Antofagasta M_w 8.0 earthquake [*Husen et al.*, 1999].

2. Wide-Angle Data

[7] Within the framework of the experiment Crustal Investigations Off- and Onshore Nazca/Central Andes (CINCA) in 1995 with German R/V *SONNE* (cruise 104) several offshore wide-angle seismic profiles were recorded with Ocean Bottom Hydrophones (OBH) and onshore stations. The gross seismic structure of the margin was modeled from land explosions and air gun shots recorded only on land stations along nine refraction profiles [*Patzwald et al.*, 1999]. However, the data from the Ocean Bottom Hydrophones (OBH) deployed along the continental slope in the northernmost profiles were not included in that modeling. In this work, we have used data from profile SO104-401 recorded with 15 OBHs (IFM-GEOMAR) and 4 PDAS land stations (GFZ-Postdam) deployed along a ~225-km-long transect extending from the outer rise of the oceanic plate to the western segment of the emerged forearc, across the trench axis and continental slope (Figure 1). Receiver spacing along the profile ranges between 6 and 12 km. Three 30-L air guns were shot from R/V *SONNE*, every 60 s (~150 m) from near the coast to well on to the outer rise (Figure 1).

[8] The record sections obtained at five OBHs and two land stations are shown in Figure 2. Sections are shown after predictive deconvolution, 3–13 Hz Butterworth filtering, equalization, and Automatic Gain Control. Signal-to-noise ratio obtained in most of the sections is low. Intracrustal diving waves (P_g) are observed at offsets less than 40 km from the source. Seismic arrivals are observed at shorter offsets at OBHs located at the lower and middle slope than at OBHs located at upper slope and land stations (e.g., Figures 2b and 2f). P_g phase shows apparent velocities that range from 3–4 km/s in the lower slope (Figure 2b) to 5–6 km/s in the upper slope (Figure 2e), revealing a significant lateral velocity gradient within the upper plate. Another phase observed in most instruments is a prominent reflection confined to a small segment of the record section that has been associated to a phase reflected at the interplate boundary zone (P_iP). Consistently, P_iP is recorded later at OBHs in the upper slope and at land stations than at OBHs in the lower slope (e.g., Figures 2b and 2f). Data from OBHs located on the oceanic plate are less clear. In these OBHs, P_g is observed only up to ~25 km offset, and the P_n is an indistinct event followed up to ~50 km offset (Figure 2a). Signal-to-noise ratio is higher in records from land stations, but P_g and P_iP phases are observed at similar offsets and with similar amplitudes than at OBH records. Land stations show however an additional refracted phase observed up to more than 150 km offset. This phase displays an apparent velocity of >8.0 km/s, and thus it has been interpreted as a diving wave traveling within the upper oceanic mantle (P_n). The long offset of P_n recordings contrasts with the limited propagation of P_g, indicating that P_g energy decay is probably not related to site effects, but more likely to the existence of an intracrustal shadow zone within the upper plate. Significance of the shadow (or low velocity) zone is addressed in the discussion section.

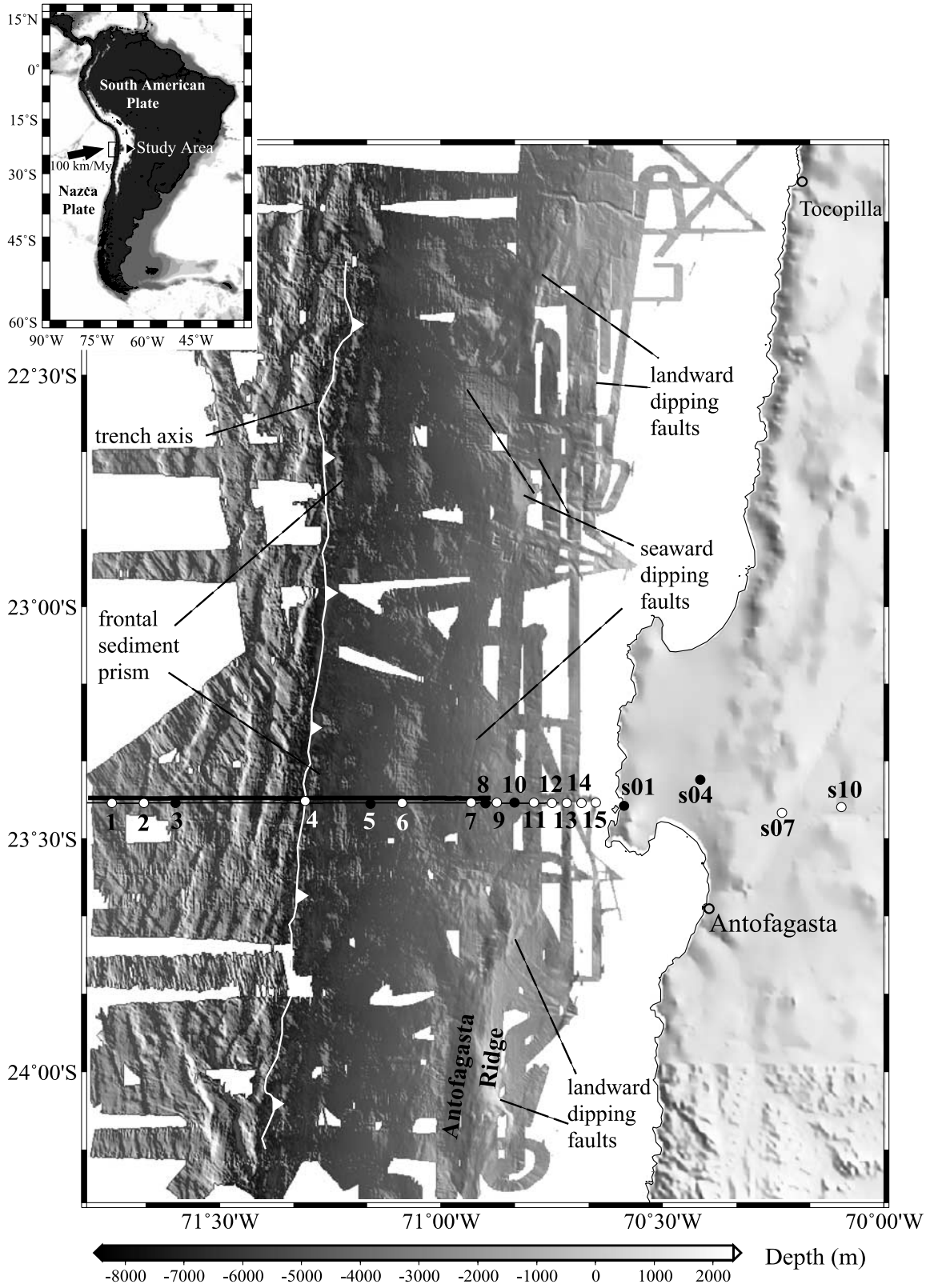

Figure 1. Shaded relief map of the multibeam bathymetry offshore of the Antofagasta sector of northern Chile. Inset shows a regional location map. The arrow displays the convergence direction of the Nazca plate with respect to the South American plate. Thick line is the track of the seismic reflection profile, and thinner line indicates the extent of wide-angle shooting and gravity data acquired offshore Mejillones peninsula. Circles indicate ocean bottom hydrophones and land stations used in the seismic modeling. The record sections of the instruments indicated by solid circles are shown in Figure 2. See color version of this figure at back of this issue.

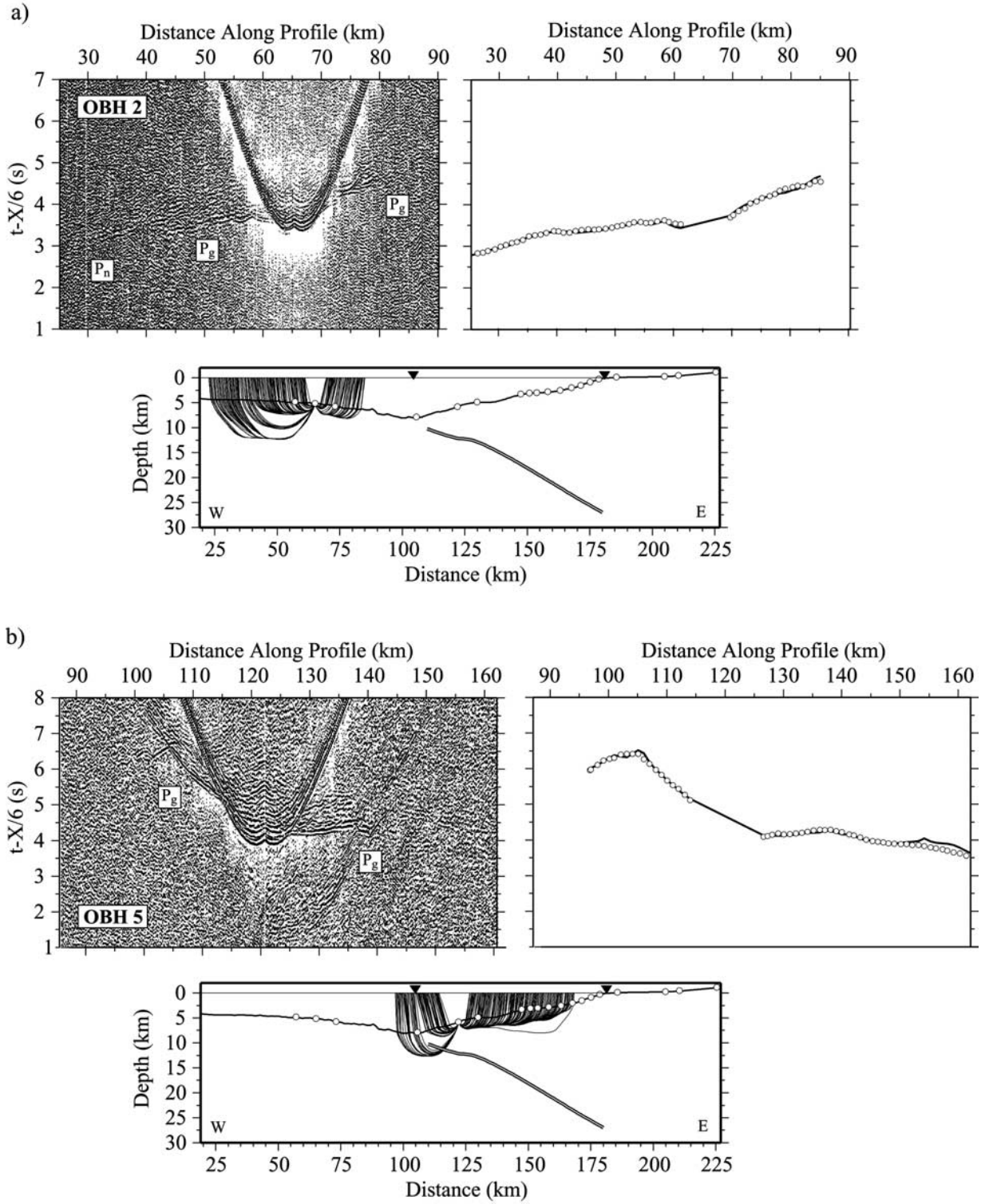

Figure 2. Record sections of the instruments displayed in Figure 1. Systematic data processing consisting of predictive deconvolution, 5–15 Hz Butterworth filtering, and automatic gain correction, applied to all the gathers, is shown in the top left plots in Figures 2a–2e and the top plots in Figures 2f and 2g. Picked travel times (solid line) and predicted travel times (open circles) for P_g, P_n, and P_iP phases using the velocity models displayed in Figure 4a are shown in the top right plots in Figures 2a–2e and the middle plots in Figures 2f and 2g. Ray tracing corresponding to the same seismic phases is shown in the bottom plots for Figures 2a–2g. Arrows show the location of the trench and the coastline. (a) OBH 2, (b) OBH 5, (c) OBH 8, (d) OBH 10, (e) OBH 12, (f) land station s01, and (g) land station s04.

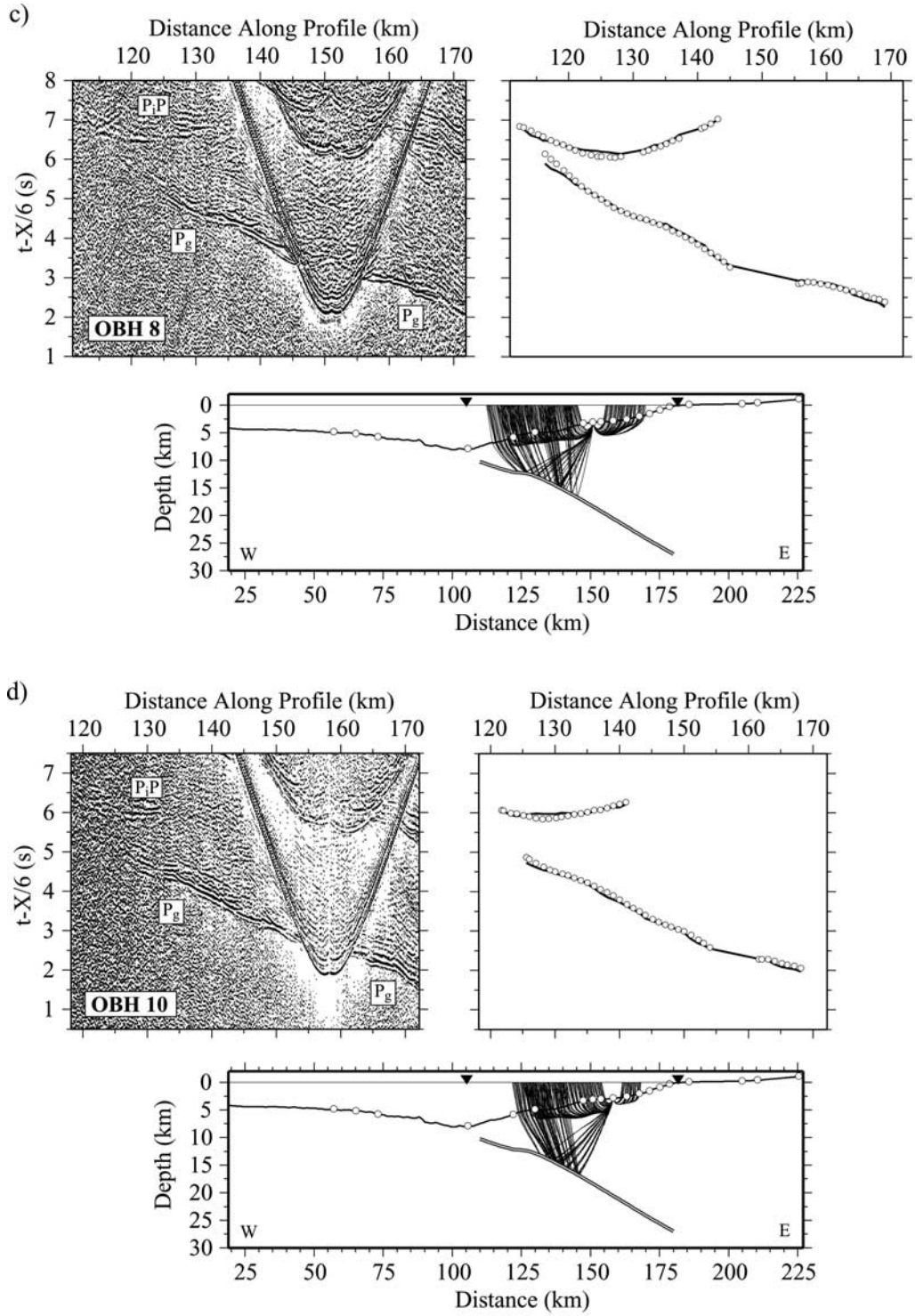

Figure 2. (continued)

[9] Consistency of P_g and P_iP phases identified in the different seismic records was checked by comparing the reciprocity of travel times for all possible source-receiver pairs. Picking of the seismic phases was done manually, and picking errors were assigned on the basis of the dominant period of the phase. A total of 3048 first arrivals (P_g and P_n), and 721 interplate reflections (P_iP) were picked from the 19 record sections. Typically, errors were assumed to be half a period of one arrival, to account for a possible systematic shift in the arrival identification, and were down weighted or over weighted according to the phase quality. Average picking uncertainties are ~50 ms at near offsets and ~60 ms at far offsets for first arrivals, and ~80 ms for P_iP.

3. Seismic Tomography

[10] The velocity-depth model along the profile was estimated using the joint refraction and reflection travel

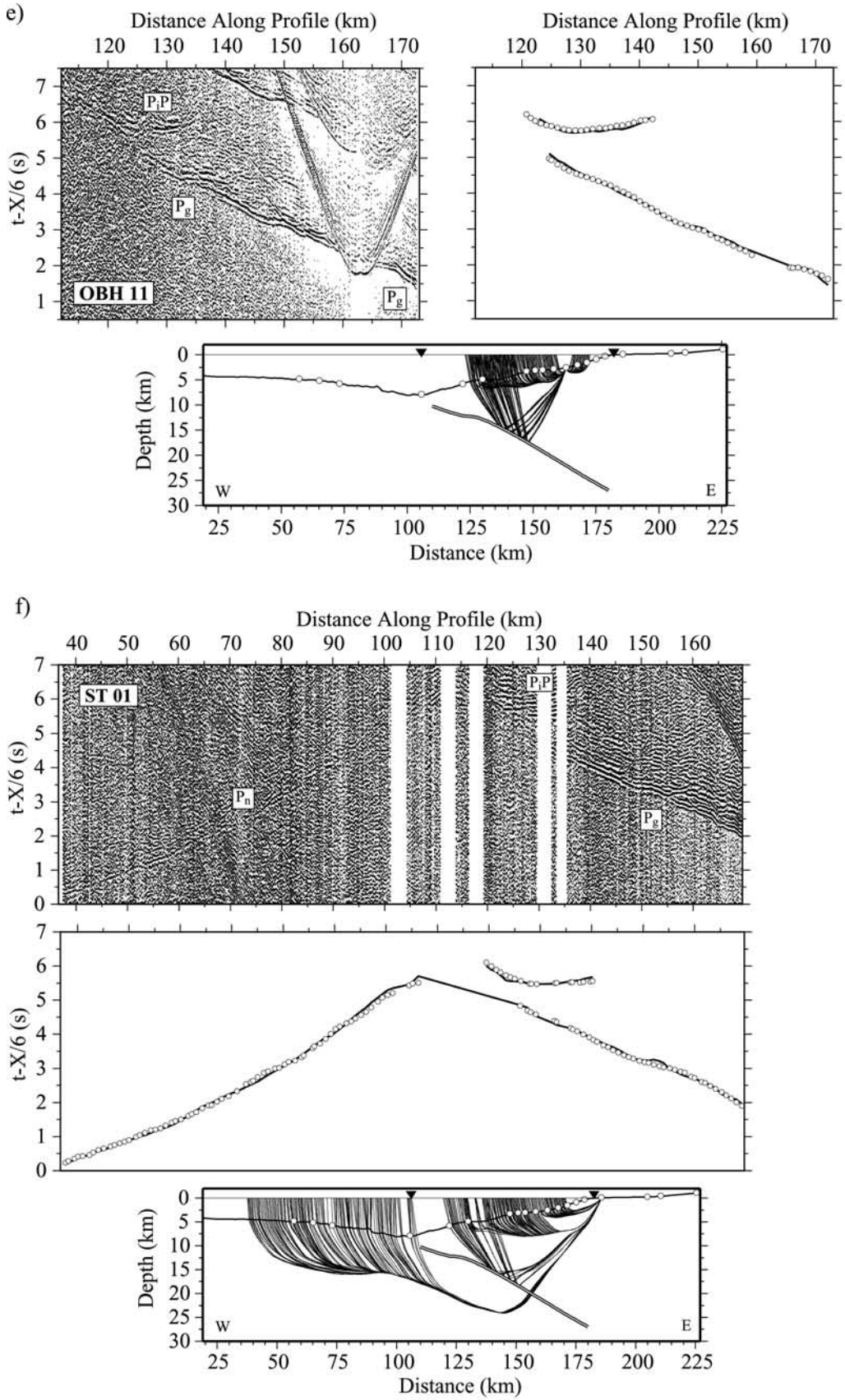

Figure 2. (continued)

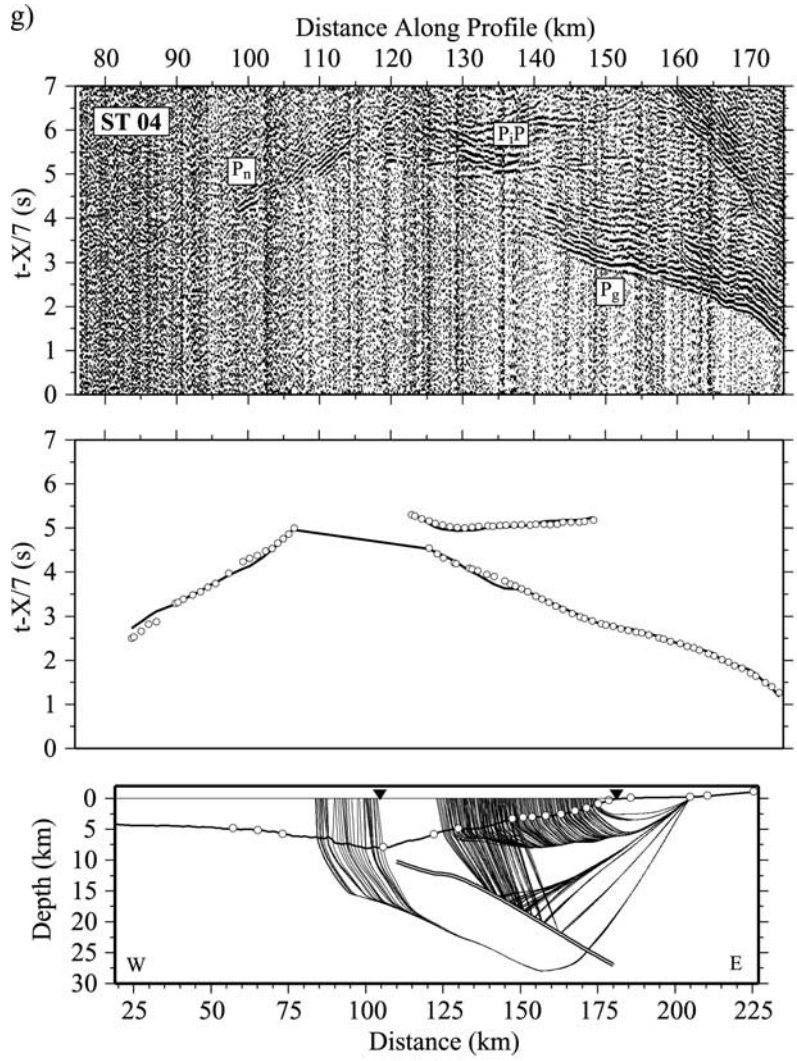

Figure 2. (continued)

time inversion method of *Korenaga et al.* [2000]. This method allows determining a 2-D velocity field together with the geometry of a floating reflector from the simultaneous inversion of first arrivals and reflections travel times. The 2-D velocity field is parameterized as a mesh of nodes hanging from the seafloor, in which node spacing can vary laterally and vertically. The floating reflector is represented as an independent array of linear segments with only one degree of freedom (vertical) for each reflector node. Travel times and ray paths are calculated employing a hybrid method based on the graph method with a ray-bending refinement [*van Avendonk et al.*, 1998]. Smoothing constraints are applied on both velocity and depth perturbations using predefined correlation lengths in order to regularize the linear system and to stabilize the inversion. Additional damping constraints are also added to the regularized linear system in a manner similar to that of *van Avendonk et al.* [1998]. For a thorough description of the method and parameters involved, see *Korenaga et al.* [2000].

[11] In this section, we first describe the construction of the reference velocity model based on the OBH data, then we specify the parameters used in the inversion process, and finally the resulting velocity model, discussing the uncertainty limits of the model parameters in the different sectors of the transect.

3.1. Reference Model and Inversion Parameters

[12] The 2-D velocity model is 225 km long and 30 km deep. The floating reflector was used to model the interplate boundary beneath the continental margin. The initial geometry of the interplate boundary reflector corresponds to that obtained in the prestack depth-migrated section of the MCS profile beneath the slope [*von Huene and Ranero*, 2003], and to the seismogenic zone defined by well-located aftershocks of the 1995 Antofagasta earthquake that nucleated beneath the shelf and coastal area [*Husen et al.*, 2000]. The 2-D reference velocity model is composed by (1) an oceanic plate section, which is the 1-D velocity model that best fits the bathymetry-corrected travel times of P_g and P_n arrivals from the three OBS located over the oceanic plate (Figure 1) [*Ranero and Sallarès*, 2004], and (2) two continental margin sections, which correspond to the 1-D velocity models that best fit P_g and P_iP travel times from OBHs located at the lower slope (OBHs 4–8 in Figure 1) and upper slope (OBHs 9–15 in Figure 1), respectively. The seismic velocities of the reference model of the upper plate are calculated

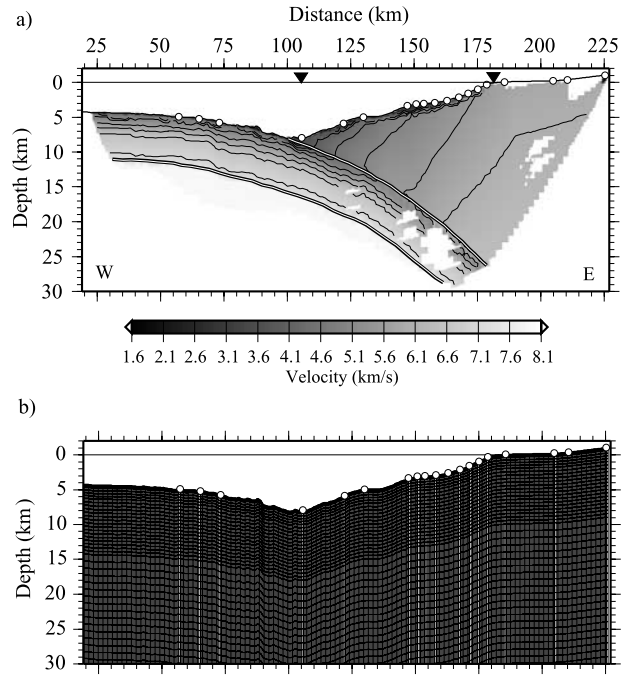

Figure 3. (a) Initial velocity model used as a reference for the Monte Carlo analysis and for velocity inversion. The model was obtained by linearly interpolating velocities of the 1-D velocity models obtained in the upper and lower slopes. Average P_iP travel times are also used to estimate the depth of interplate boundary beneath the midslope. The model of the oceanic plate was extended laterally to beneath the interplate boundary landward of the trench axis. Arrows show the location of the trench and the coastline. (b) Mesh of nodes used for calculation of ray paths and travel times.

by linearly interpolating the velocities of the two 1-D velocity models. Average P_iP travel times are also used to estimate the depth of interplate boundary beneath the mid slope. The model of the oceanic plate has been extended laterally to beneath the interplate boundary landward of the trench axis (Figure 3a). The root mean square (rms) travel time residuals obtained with the 2-D reference model are 351 ms for first arrivals and 179 ms for P_iP. Horizontal grid spacing of the model used for velocity inversion is 0.5 km, whereas vertical grid spacing is varied from 0.1 km at the top of the model to 1 km at the bottom (Figure 3b). Depth nodes defining the interplate reflector are 1 km spaced. We used horizontal correlation lengths ranging from 8 km at the top to 15 km at the bottom of the model, and vertical correlation lengths varying from 0.4 km at the top to 2.5 km at the bottom. Different tests showed that varying 50% this value does not affect significantly the solution. Depth and velocity nodes are equally weighted in the P_iP travel time inversion. The 2-D velocity model and reflector geometry obtained after 10 iterations of the inversion process are shown in Figure 4a. Rms residuals obtained using this model are 62 ms for first arrivals ($\chi^2 = 1.5$) and 82 ms for P_iP ($\chi^2 = 1.1$). Picked and calculated travel times, and ray tracing from five OBHs and two land stations are shown in Figures 2a–2g. The derivative weight sum (DWS), which is the column sum vector of the velocity kernel [*Toomey and Foulger*, 1989] and provides crude information on the linear sensitivity of the inversion, is shown in Figure 4b.

3.2. Seismic Structure

[13] The resultant 2-D velocity model (Figure 4a) has two different regions. One is the oceanic plate section westward of the trench axis, with crust ~7.0 km thick, consistent with the 6.87 ± 0.29 km average thickness of Pacific plate crust older than 30 m.y. from the data compilation of *White et al.* [1992]. In the outer rise, upper crustal velocities increase rapidly from <4 km/s at the top of the basement to ~6.5 km/s at 3.0–3.5 km below seafloor. Lower crustal velocities increase steadily to ~7.3 km/s at the crust-mantle boundary. Closer to the trench intracrustal velocities are as much as 0.5 km/s lower than in the outer rise, which means that they are much lower than those of the average Pacific crust. The trenchward decrease of oceanic crustal velocities was previously recognized from modeling of the seismic records of the three OBHs on the oceanic plate (OBHs 1, 2, and 3 in Figure 1), and interpreted as evidence that the Nazca plate at the north Chile trench is pervasively faulted and hydrated [*Ranero and Sallarès*, 2004]. The upper mantle velocity is also low (~7.5–7.7 km/s), suggesting that bending-related faulting allows fluids to percolate deep and serpentinize mantle peridotite [*Ranero and Sallarès*, 2004]. Beneath the continental slope, crustal and upper mantle velocities of the subducting plate are constrained by diving waves (P_n) recorded only at the land stations. In this sector the velocity resolution of the oceanic crust and mantle is low and the velocity obtained from the inversion depends largely on the input velocity in the reference model. This is discussed with more detail in the next section.

[14] The second region is the overriding plate, which shows well-constrained and significant lateral and vertical gradients in seismic velocity. Velocity is as low as ~3.5 km/s at the edge of the margin, increasing at a rate of ~0.02 s^{-1} beneath the lower slope. Low velocities (~3.0 km/s) are also obtained in the first ~1 km beneath the slope, but they rapidly increase downward at ~0.8 s^{-1}. A remarkable feature observed along much of the margin is a subhorizontal low-velocity zone showing a velocity contrast of as much as ~0.3 km/s. The velocity inversion occurs at ~7 km depth between ~30 km from the trench and the coastline and is 2–3 km thick. The resolvability of such a low-velocity zone given the experiment geometry is discussed in the next section. Below this zone velocities increase only slightly with depth. The higher velocities of the upper plate (~6.5 km/s) are obtained near the bottom, just beneath the coastline. Shallow velocities are higher onshore, with a small vertical velocity gradient, than offshore. The dip angle of the subducting slab, determined essentially from P_iP reflections, is ~8° beneath the lower continental slope, rapidly increasing to ~16° beneath the mid slope in good agreement with MCS results [*von Huene and Ranero*, 2003]. The interplate boundary dips from ~10 km depth beneath the lower slope to ~25 km depth beneath the coastline, equivalent to an average dip angle of 12°.

3.3. Model Uncertainty and Sensitivity Tests

[15] Velocity uncertainty of the model parameters in the oceanic plate section has been estimated by performing a Monte Carlo–type analysis. The results for the uncertainty

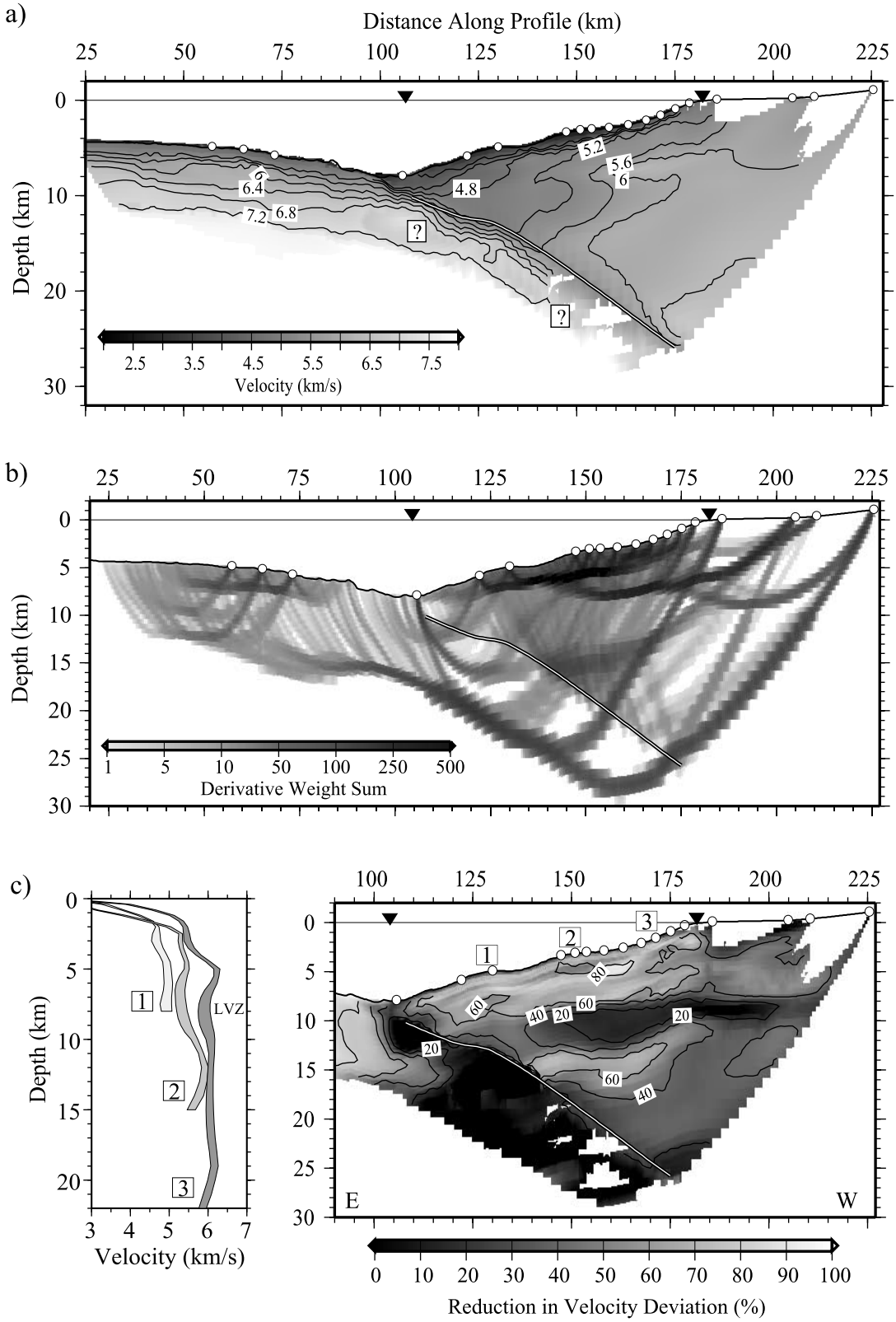

Figure 4. (a) Final velocity model with isovelocity contours. Thick white line shows location of the interplate boundary derived from inversion of P_iP reflection travel times. White circles indicate OBH and land stations locations. Arrows show the location of the trench and the coastline. (b) Derivative weight sum (DWS). (c) (right) Improvement of mean deviation of all the Monte Carlo realizations with respect to the reference velocity models. Numbers indicate location of the 1-D velocity profiles shown in Figure 4c (left). (left) The 1-D velocity profiles. The shaded area shows the horizontally averaged velocity deviation estimated from the Monte Carlo analysis. See color version of this figure at back of this issue.

analysis of the oceanic plate before subduction are discussed by *Ranero and Sallarès* [2004], and here we center the analysis on the estimation of velocity uncertainty of the upper plate structure, the main focus of this work. The procedure to estimate velocity uncertainties consisted on randomly perturbing velocities ($\sigma_v = 0.35$ km/s) of the upper and lower continental slope 1-D reference models (see section 3.1) and to combine them in order to generate a set of 100 different initial 2-D reference models. Together with the perturbed reference models we used 100 noisy data sets constructed by adding random common phase errors (±50 ms) and common receiver errors (±50 ms) to the initial data set [*Korenaga et al.*, 2000]. Then we performed a tomographic inversion for each velocity model with a noisy data set, in order to estimate not only the dependence of the solution on the reference model but also the effect of phase arrival picking errors. The mean deviation of all realizations of such an ensemble is considered to be a statistical measure of the model parameters uncertainties [*Tarantola*, 1987]. This type of Monte Carlo analysis is similar to that performed by *Sallarès et al.* [2003, 2005].

[16] Velocity deviations are smaller than 0.1 km/s in the shallow ∼2–3 km of the upper plate, increasing to 0.15–0.20 km/s to 5–6 km depth beneath the seafloor. Underneath, velocity uncertainty is somewhat higher (∼0.25 km/s) in the low-velocity area that separates the lower and upper domains, indicating that absolute velocities are worst constrained in this part of the upper plate. Velocity uncertainty improves again beneath the low-velocity zone to 0.15–0.2 km/s across the lower area of the upper plate, to close to the plate boundary, where velocities are also poorly constrained. Figure 4c shows the reduction, or improvement, of the mean deviation of the 100 final velocity models with respect to the mean deviation of the reference ones. Deviation reduction is significant at all crustal levels. In the upper half, reduction is 70–80%, indicating that in this sector we obtain very similar velocities independently of the velocities considered in the reference model. Below the low-velocity zone, the deviation reduction is 50–60%, decreasing to less than 40% near the interplate boundary zone. The lowest deviation reduction is obtained at the low-velocity zone. Here the reduction of the velocity deviation is only 20–40%, indicating that absolute velocities are not well constrained and that the velocity in the model is only approximate. As observed in Figure 4c, the velocity of the oceanic plate underneath the margin is largely unconstrained. Figure 4c displays also an inset with three 1-D velocity-depth profiles extracted from the velocity model shown in Figure 4a at 130, 150, and 170 km along profile with the uncertainty bounds corresponding to the mean deviation of the Monte Carlo realizations. The inset shows that the velocity inversion occurs systematically, independently of the initial velocity model considered.

[17] We have performed an additional test with synthetic data in order to check the resolvability of the low-velocity zone provided the experiment geometry. For this, we have created two synthetic models consisting of a single sinusoidal anomaly located between 6.5 km and 9.5 km depth and 110 km and 180 km along profile (i.e., the location of the low-velocity zone), superimposed onto the final velocity model of Figure 4a. The maximum amplitude of the anomaly in the two synthetic models is respectively +5% and −5% of the background velocity (Figures 5a and 5d). Synthetic noisy data with the same source-receiver geometry as in the real data set have been generated for the two models. The result of the inversions starting from the reference model of Figure 3a and using the synthetic data set and the differences between the synthetic and inverted models are shown in Figure 5. The results show that both the location and amplitude of the velocity anomaly are reasonably well recovered within uncertainty limits in the two models, indicating that the experiment geometry and data set allow discerning between positive and negative velocity variations at 6.5–9.5 km depth. The sensitivity of the data is therefore sufficient to resolve structures with size and amplitude similar to the low-velocity zone at this depth range (Figure 5), which implies that the velocity inversion shown in Figure 4a is not an artifact of the inversion procedure but a real feature.

4. Seismic Velocity-Derived Geophysical Models

[18] A major issue to infer the nature of the crust using seismic velocities only is that different rock types may display very similar P wave velocities. It is well known that the P wave to S wave velocity ratio is more sensitive to the presence of heterogeneities and fluids than P wave velocities only [e.g., *Husen and Kissling*, 2001]. Given that no information on S wave velocity is available in our case, we have combined velocity and gravity modeling to circumvent this issue. Most rock types show typically a specific correlation between compressional wave velocity and density. Velocity-density relations, which are principally based on empirical observations valid for a given rock, hold then key information to discriminate between different rock types by means of gravity analysis [e.g., *Sallarès et al.*, 2001]. They can be crudely categorized as those valid for sediments [e.g., *Hamilton*, 1978], continental rocks [e.g., *Christensen and Mooney*, 1995], and oceanic crust [*Birch*, 1961; *Christensen and Salisbury*, 1975; *Carlson and Herrick*, 1990]. Our strategy consisted on constraining first the margin's rock composition through gravity modeling of velocity-derived density assuming a homogeneous composition for the overriding plate, and subsequently estimating porosity and fluid content based on a velocity-porosity conversion relation. Since this approach is only viable when the average rock composition is well constrained from velocity and density, we have propagated the Monte Carlo–based velocity uncertainties to density and porosity calculations to see if the differences between models for different compositions are resolvable.

4.1. Density Model

[19] The high-resolution shipborne gravity data along the seismic transect was acquired during the CINCA experiment. Gravity modeling was performed using a code based on *Parker*'s [1972] spectral method, which makes it possible to calculate the gravity anomaly produced by a heterogeneous 2-D density model [*Korenaga et al.*, 2001]. Seismic velocity (Figure 4a) was converted to density using two different velocity (v)–density (ρ) empirical relations. In the two cases, the uncertainty of the velocity model (Figure 4c) is propagated to that of the calculated gravity anomaly on the basis of the 100 Monte Carlo ensembles.

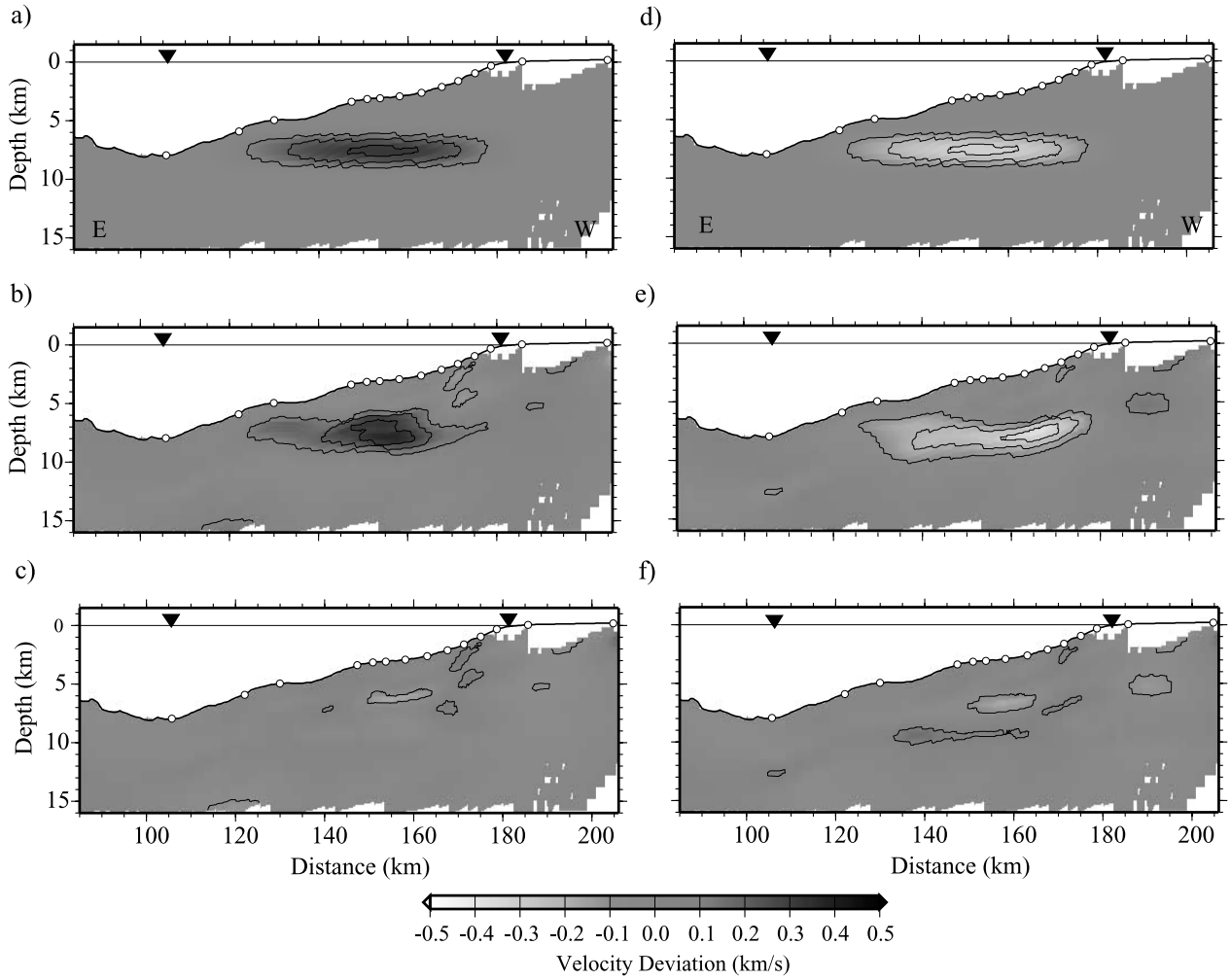

Figure 5. Results of the checkerboard test. (a and d) Synthetic reference velocity models, consisting of a single sinusoidal anomaly of −5% and +5%, respectively, superimposed onto the final velocity model of Figure 4a. (b and e) Inverted models using velocity model of Figure 3a as initial model and the synthetic noisy data sets. (c and f) Difference between reference and inverted velocity models. Arrows show the location of the trench and the coastline.

For the oceanic plate we used *Carlson and Herrick*'s [1990] relation, $\rho = 3.81 - 6.0/v$, which is based on Deep Sea Drilling Project (DSDP) and Ocean Drilling Program (ODP) core data. Because the oceanic plate has less than 100 m of sediment the same empirical relation was applied to the entire crust. Oceanic upper mantle density was fixed to 3.3 g/cm^3. In a first model (model A), we used *Christensen and Mooney*'s [1995] nonlinear v-ρ regression curve, $\rho = 4.93 - 13.29/v$, for the continental upper plate. This relation is considered to be adequate for all continental rock types at a pressure equivalent to 10 km depth. The continental slope off Antofagasta is largely sediment starved [e.g., *Hartley and Chong*, 2002] exhibiting only few small sedimentary basins in the upper slope and a thin veneer of sediment across the middle slope [*von Huene and Ranero*, 2003], thus the same relation was applied to the entire upper plate. This approach assumes that large velocity gradients within the upper plate are predominantly due to variations in porosity and/or rock alteration. Model A underestimates the observed anomaly landward of the trench axis (Figure 6b), indicating that the 10-km depth v-ρ conversion law for continental rocks is not adequate. The RMS misfit for this model is 15.2 mGal. A similar misfit occurs using the 20-km depth relation [*Christensen and Mooney*, 1995]. A second model of the continental margin (model B) was constructed using *Carlson and Herrick*'s [1990] empirical curve for oceanic crust. Model B accounts much better for the gravity anomaly across the entire continental slope (Figure 6b). The misfit between observed and calculated anomaly is 5.1 mGal, three times smaller than that obtained using *Christensen and Mooney*'s [1995] curve of velocity-density relation, indicating that the basement of the upper plate must be mostly composed of basalt-type rocks. A third model (model C) maintains the densities of model B for the oceanic plate crust and the upper plate, but the density of the oceanic upper mantle was reduced to 3.15 g/cm^3. Model C with the anomalously low mantle density (Figure 6a) gives the lowest rms, 3.2 mGal (Figure 6b). Uncertainties of the calculated gravity anomalies propagated from averaging of the Monte Carlo ensembles are lower than 10 mGal for the

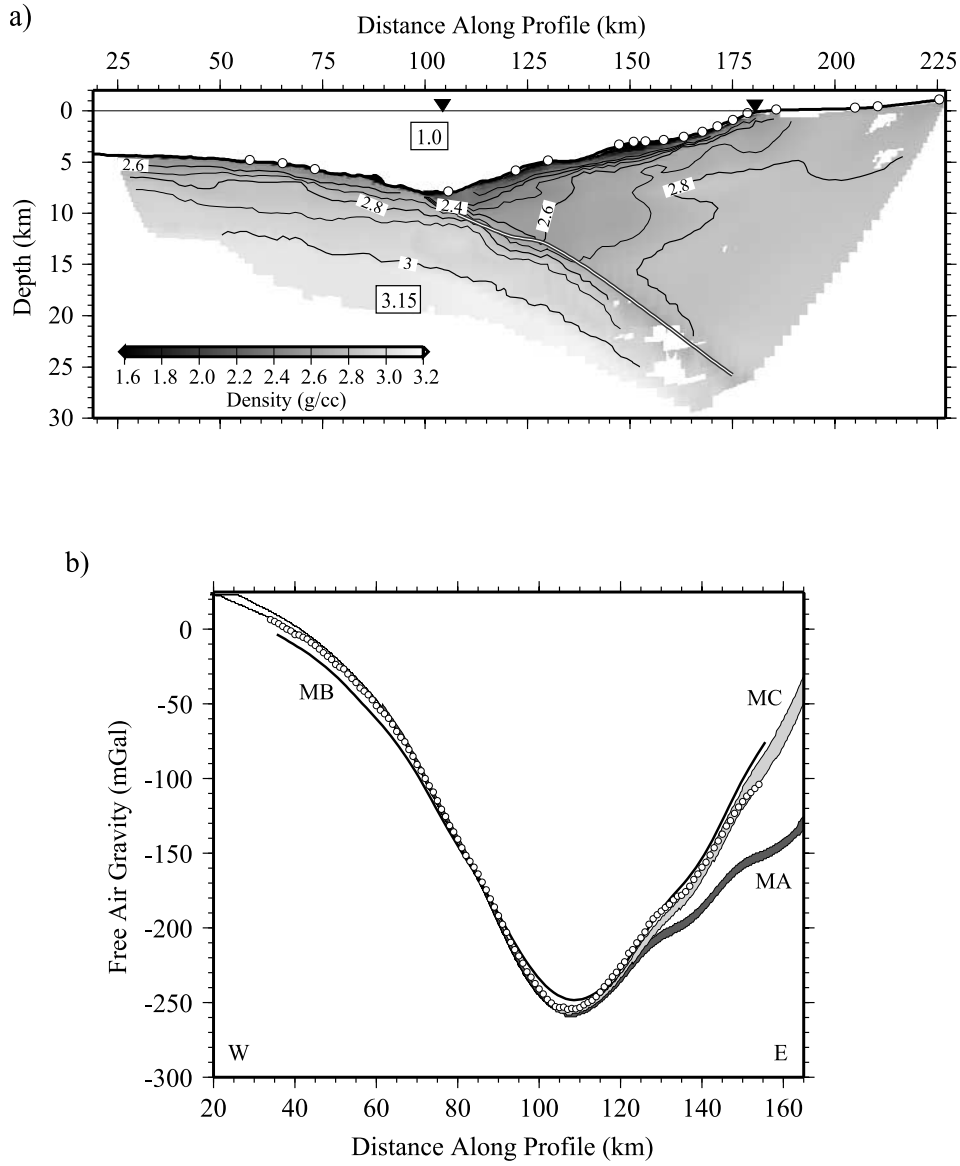

Figure 6. (a) Density model along the transect derived from the velocity model displayed in Figure 4a. Density is expressed in g/cm^3. Arrows show the location of the trench and the coastline. (b) Observed free-air gravity anomaly (open circles) and calculated gravity anomaly for different density models. Light gray dashed area (MC) is the gravity anomaly calculated with the model displayed in Figure 6a (model C in the text). The thickness of the shaded area corresponds to the Monte Carlo–based uncertainty limits. In this model we used *Carlson and Herrick*'s [1990] *v*-ρ empirical relation for oceanic crust. The RMS residual obtained with this model is 3.2 mGal. Solid line (MB) was obtained using the same *v*-*r* conversion law but with a mantle density of 3.3 g/cm^3 (model B in the text). RMS is 5.1 mGal. Dark gray shaded area (MA) was obtained using *Christensen and Mooney*'s [1995] *v*-ρ conversion relation for continental crust (model A in the text). RMS is 15.2 mGal.

upper plate, evidencing that differences between the density models considered here are resolvable with this approach (Figure 6b). The low mantle densities inferred from gravity modeling support the limited information provided by the wide-angle seismic data indicating that the upper oceanic mantle also has anomalously low velocities. A plausible explanation of the low densities and velocities is the serpentinization of the upper mantle peridotite by water percolating through the normal faults formed during plate bending into the trench [*Ranero et al.*, 2003; *Ranero and Sallarès*, 2004].

4.2. Porosity and Strength of the Upper Plate

[20] A number of relations connecting the physical properties of rocks (e.g., seismic velocity, density) with their porosity (ø) and porosity-related properties (e.g., permeability, strength, saturation) have been proposed in recent years, in step with advances in seismic methods and interpreta-

tions. The inferences most commonly used can be classified in (1) empirical relations that are obtained statistically for a given data set [see *Mavko et al.*, 1998], (2) bounds that are rigorously derived from basic physical principles but do not give specific velocity estimates, only a range of possible values [e.g., *Hashin and Shtrikman*, 1963], and (3) "naïve" deterministic models that attempt a meaningful explanation of the experimental observations [e.g., *Wyllie et al.*, 1956; *Raymer et al.*, 1980]. Empirical relations for water-saturated sediment are numerous (see review by *Erickson and Jarrard* [1998]), but are scarce for crystalline rocks. In the latter case, naïve deterministic models and bounds are most commonly used to estimate porosity from velocity. Most models assume that rocks behave identically regardless of the porosity volume (i.e., they are frame supported). A primary achievement of rock physics during the last decade has been, however, to demonstrate that this is not the situation. At porosities higher than a given threshold value (e.g., 30–40% for sediments), intergrain contacts are too weak to transmit applied load and the strength of the rock is low. Under those conditions the rock is disaggregated and behaves as a suspension (fluid supported). In this domain, seismic velocity is essentially not sensitive to changes in porosity. Below the porosity threshold the rock is frame supported, it is able to transmit loads and velocity is highly sensitive to porosity (see review by *Nur et al.* [1998]). *Nur et al.* [1991] referred to this threshold porosity value as critical porosity (ϕ_c). All types of rocks exhibit a critical porosity value, which can be as low as 5% for cracked igneous rocks [*Nur et al.*, 1998]. For water-saturated basalt, representative of deep sea oceanic crust, the critical porosity is 10–15% (Figure 7). Several effective medium theories incorporating the concept of critical porosity have recently emerged [e.g., *Mukerji et al.*, 1995]. Modifications typically made include the replacement of the inclusion phase by the critical phase and the renormalization of the porosity to ϕ/ϕ_c. A simple example of a critical porosity effective medium theory is the modified Voigt bound, which apparently provides a good estimate for velocities at porosities below ϕ_c [*Nur et al.*, 1998]. In this circumstance, the original Voigt bound (i.e., a linear interpolation between the elastic properties of two constituents of a two-phase composite) is modified by replacing the water end-member (at 100% porosity) by the suspension end-member (at ϕ_c). By doing so, porosities below ϕ_c can be estimated from the compressional wave velocity, v, as follows:

$$\Phi = \left[\frac{v_R - v}{v_R - v_S}\right]\Phi_c, \qquad \text{for } \phi < \phi_c, \tag{1}$$

where v_R the velocity of the bulk rock and v_S is the velocity of the suspension, which in turn can be approximated calculating the lower Reuss bound at the critical porosity:

$$v_S = \left[\frac{(1-\Phi_c)}{v_R} + \frac{\Phi_c}{v_w}\right]^{-1}, \tag{2}$$

where v_w is water velocity.

[21] Figure 7 shows the compressional wave modulus, or M modulus ($M = \rho v^2$, where ρ is density) as a function of porosity for water-saturated basalt, based on experimental data extracted from the work of *Nur et al.* [1998]. If we use *Carlson and Herrick*'s [1990] relation for v-ρ conversion, $\rho = 3.81 - 6.0/v$, as we did in the gravity analysis, it is possible to express M in terms of v only:

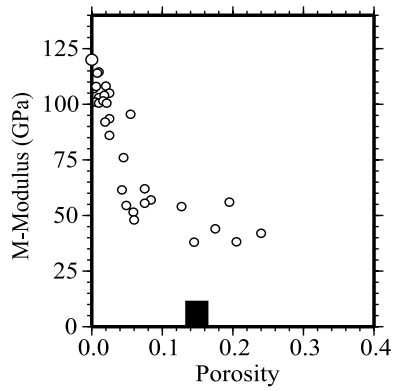

Figure 7. M modulus–porosity diagram for water-saturated basalts. Black tick indicates the critical porosity (Φ_c) estimated for this particular data set. Data are from *Nur et al.* [1998].

$$M = 3.81v^2 - 6.0v. \tag{3}$$

[22] As is observed in Figure 7, the M modulus for zero-porosity basalt, M_R, is ~120 GPa, which based on (3) corresponds to a velocity, $v_R \approx 6.5$ km/s. This velocity is typical of lower oceanic crust, where porosity is believed to be negligible, and is similar to the velocity at the bottom of the upper plate beneath the coastline (Figure 4a). Substituting v_R into (2) and using $\phi_c = 0.15$ (i.e., 15%), we obtain an estimate of the suspension end-member velocity for the basement of the upper plate, $v_S \approx 4.3$ km/s. The M modulus for this phase is thus $M_S \sim 43$ GPa, apparently consistent with data from Figure 7 at a porosity higher than ϕ_c. Therefore interpreting that the basement of the overriding plate is effectively made of igneous rocks similar to oceanic basalt as indicated by the v-ρ relation, then the parts of the margin with velocity lower than ~4.3 km/s ($\phi > 0.15$) would have to be made of largely disaggregated material. For velocities higher than ~4.3 km/s ($\phi < 0.15$), we can approximate the rock porosity from (1), using the values of v_R, v_S, and ϕ_c referred to above:

$$\Phi = 0.46 - 0.07v. \tag{4}$$

[23] Figure 8 shows the upper plate porosity estimated from (4), using the velocities obtained in the tomography model (Figure 4a). Porosity uncertainties propagated from the Monte Carlo–derived velocity models are smaller than 1% within most of the upper plate, and 1–2% in the low-velocity zone, being the uncertainties negligible for the comparison of material physical properties and tectonic processes.

5. Discussion

[24] In this section we integrate the velocity and density information with the structure imaged by MCS data, the

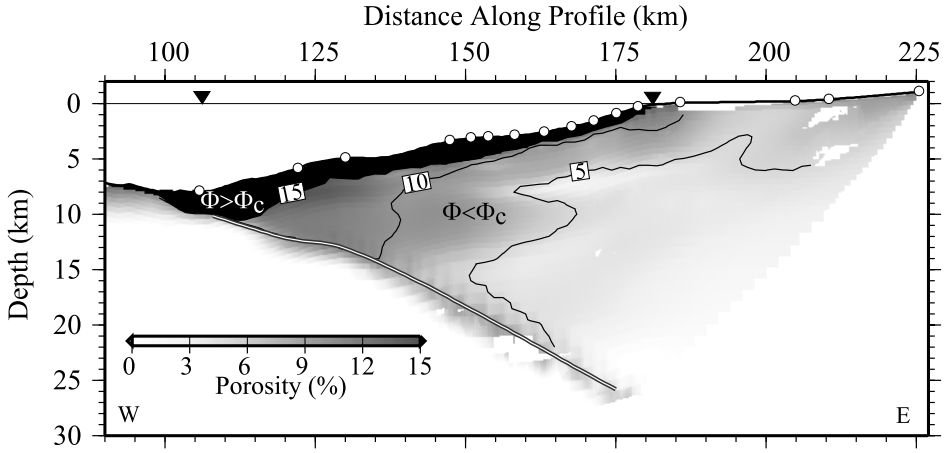

Figure 8. Porosity model calculated using the seismic velocity model displayed in Figure 4a. Porosities above critical are shown in black. Arrows show the location of the trench and the coastline.

porosity distribution, and the extent of the rupture zone of the Antofagasta M_w = 8.0 earthquake, to infer the nature of the overriding plate and the relation between physical properties and long-term and short-term (earthquakes) tectonic processes.

5.1. Nature of the Overriding Plate

[25] The upper plate has seismic velocity and density values characteristic of basalt-type rocks rather than granitic or sedimentary rocks (see section 4.1), probably indicating that the bulk of the margin framework is composed of basaltic-andesite similar to the Jurassic magmatic arc of the La Negra formation that crops out along the coastal regions. The extension of this rock framework offshore may indicate the presence of a pre-Jurassic magmatic arc, currently submerged due to thinning and subsidence of the overriding plate caused by tectonic erosion. A similar submerged pre-Jurassic magmatic arc has been interpreted based on a margin-parallel linear trend of magnetic dipole anomalies offshore of Valparaiso at 32°–34°S [*Yañez et al.*, 2001]. Assuming that the submerged pre-Jurassic magmatic arc is continuous along >1000 km from north Chile to Valparaiso implies a large eastward migration of the magmatic arc (250–300 km) through time, consistent with long-term subduction erosion of the margin.

5.2. Tectonic Structure of the Overriding Plate

[26] The velocity and density structure of the margin (Figures 4 and 6) may indicate different rock bodies or changes in porosity and deformation styles. The comparison of the velocity structure with prestack depth migrated images shows the correspondence of the main seismic boundaries detected with the two methods and the relation between tectonic structure and velocity distribution (Figure 9).

[27] The top of the basement beneath the middle and upper slope approximately corresponds to the 3.8 km/s isovelocity contour (Figure 9). The velocity model displays a well-defined low-velocity zone a few kilometers beneath the top of the basement that extends from beneath the coastal area to the middle slope (Figure 4a), whose top corresponds to a subhorizontal event in the seismic reflection images (Figure 9). The sharp velocity decrease across this boundary indicates an abrupt change in physical properties. The subhorizontal seismic horizon has been previously interpreted as a detachment surface where block-bounding faults cutting from the seafloor into the upper plate sole out [*von Huene and Ranero*, 2003]. This surface dips gently landward, deepening from 2 km below the seafloor beneath the middle slope to ~6 km beneath the upper slope (Figure 9). Above the detachment, the size of fault-bounded basement blocks and the fault spacing decreases seaward, indicating progressively increasing extension, thinning and dismembering of the upper plate. The ~6 km thick fault blocks of the upper slope are rotated, cut and extended by new faults that progressively thin them to ~2 km beneath the middle slope, a process coeval with basal erosion that thins the upper plate from below [*von Huene and Ranero*, 2003].

[28] Velocity gradients at the bottom of the low-velocity zone are smoother than at the top. The bottom is defined by a velocity increase that is roughly coincident with a reflection in the seismic images between km 130 and 145, where it is obscured by the seafloor multiple reflection (Figure 9). However, this velocity change is poorly controlled due to low resolution of the velocity inversion in that area (Figure 4c). The detachment at the top of the low-velocity zone may represent either a rheological boundary formed along a prefaulting contact between two rock bodies of different nature or a zone of low strength related to the presence of permeating fluids. In the latter case, the occurrence of a thick low-velocity zone beneath the detachment is somewhat surprising, because rocks above the detachment are extended by brittle faulting, fractured and probably invaded by seawater and their velocity decreases rapidly from the upper to the middle slope (Figure 4a). Seawater cannot percolate down to reach the low-velocity body because faults do not cross the detachment, and the detachment surface is highly sheared and probably a boundary for fluid migration as indicated by the abrupt velocity change across it. An alternative could be the migration of fluids from the subduction channel, a process inferred from temporal variations of P wave to S wave ratio following the 1995 Antofagasta earthquake [*Husen and Kissling*, 2001]. Fluids released from the subduction channel after great earthquakes penetrate through a fracture system and might also be channeled along the landward dipping reflec-

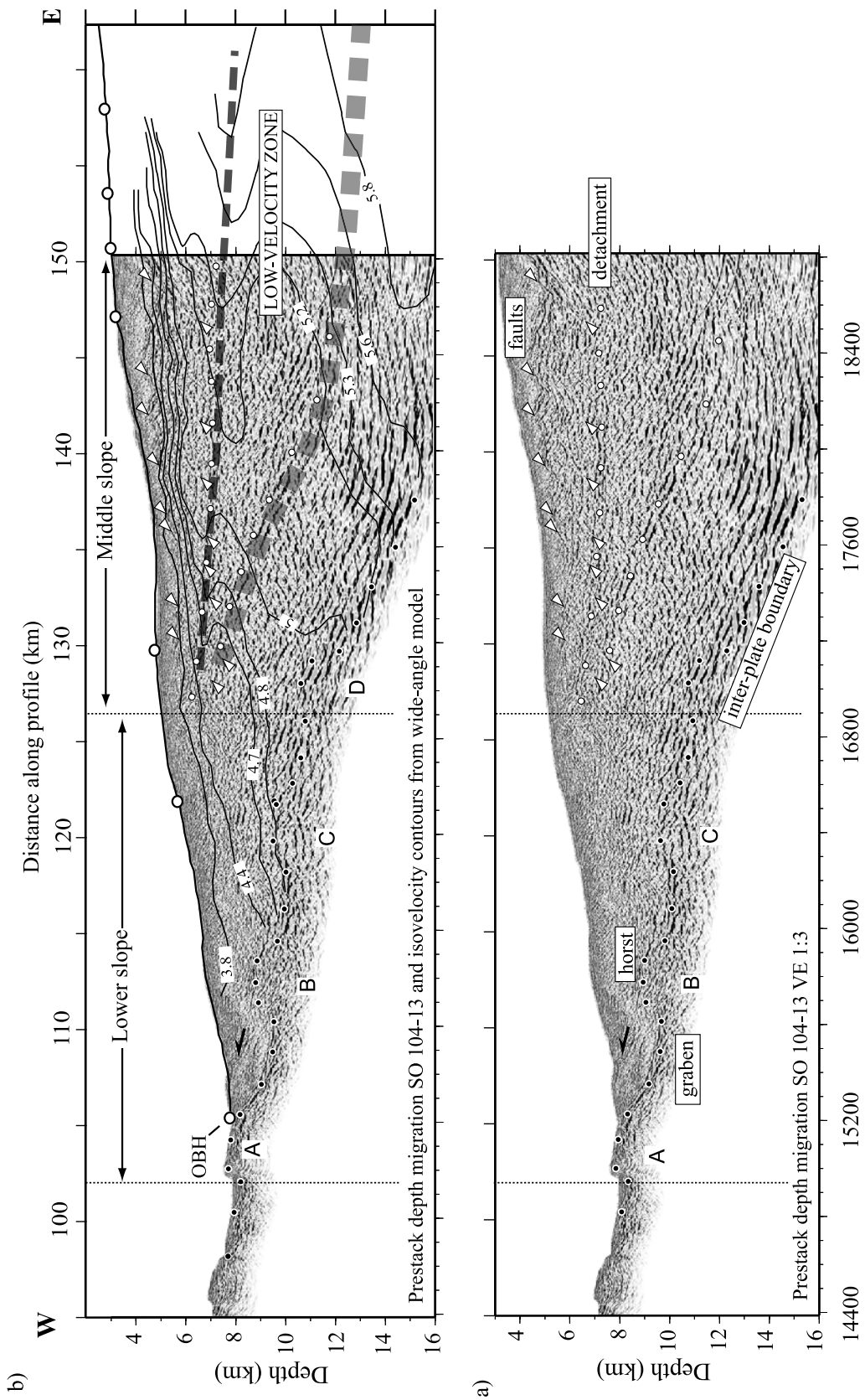

Figure 9. (a) Prestack depth migration image with tectonic interpretation [after *von Huene and Ranero*, 2003]. White dots show the intrabasement detachment and a landward dipping reflection at the base of the low-velocity zone discussed in the text. Arrows display block-bounding faults cutting from the seafloor into the upper plate. Black dots delineate the top of the subducting oceanic plate. Capital letters correspond to large subducting horsts. (b) Comparison of prestack depth migration image with tectonic interpretation and wide-angle velocity model shown as selected isovelocity contours. Thin and thick dashed lines correspond to the upper and lower bounds of the low-velocity zone, respectively.

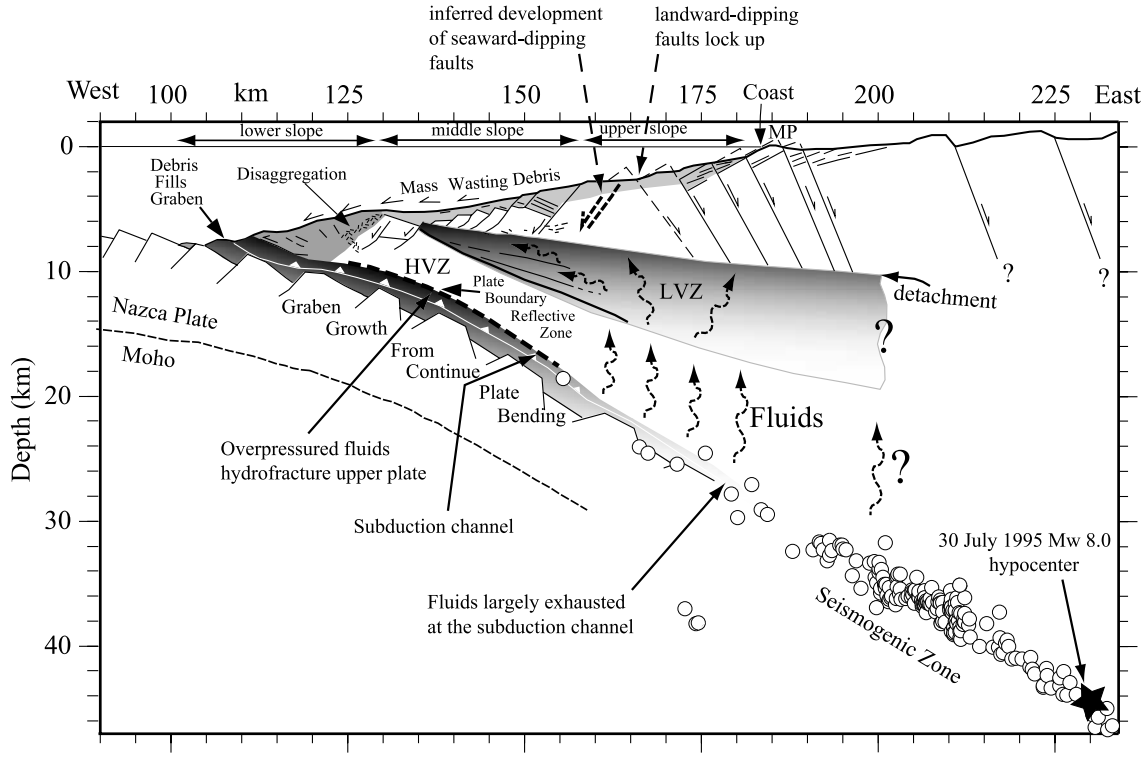

Figure 10. Interpretative model of the tectonic structure of the north Chile margin in the area of the Mejillones Peninsula. Star marks the hypocentral location of the 30 July 1995, M_w = 8.0, Antofagasta earthquake [after *Delouis et al.*, 1997], and open circles are well-located aftershocks of this event [*Husen et al.*, 1999]. MP stands for Mejillones Peninsula.

tion at about the base of the low-velocity zone, gradually collecting beneath the detachment.

[29] As discussed in section 4.2, basement rock velocities lower than ~4.3 km/s may correspond to areas with porosity larger than critical (Figure 8). The vertical velocity gradient within the upper basement is steeper in the upper slope, gradually decreasing to a gentler gradient in the middle slope, which is consistent with the progressive increasing of extensional faulting. Beneath the lower slope, where most slope sediment has been mass wasted, basement velocity is lower than 4.3 km/s (ϕ > 15%), indicating that it is probably made of disaggregated material. The downslope transition from steep to gentle vertical velocity gradients is well constrained by the velocity inversion (Figure 4c) and occurs rapidly between km 135 to 130 along profile (Figure 9). The rapid downslope change in velocity gradient is concurrent with a change in deformation style. Seismic images show that the frontal ~20 km of the overriding plate seem to be highly disrupted with pervasive deformation distributed across the plate rather than localized on individual large faults. Also, this frontal area displays along the ~200 km covered by multibeam bathymetry a series of low ridges and valleys that parallel the trend of subducting horst and graben topography of the oceanic plate (Figure 1). This morphological mimicking supports that the upper plate material lacks strength riffling over the subducting topography. The margin front is sufficiently thin to fracture and disaggregate due to repeated thrusting over subducting horsts and subsequent collapse into intervening grabens. At the toe of the margin, a <5 km wide sediment prism, formed of slope debris deposited in the trench, is thrusted and subsequently carried into the subduction channel [*von Huene and Ranero*, 2003]. Thus the frontal part of the upper plate is likely highly permeated by fluids expelled from underthrusting debris.

[30] Rock velocity in the lower part of the basement rapidly increases landward from <4 km/s beneath the lower slope to ~5 km/s beneath the middle slope and more gradually to >6 km/s beneath the upper slope (Figures 4a and 9), indicating a progressive landward decrease in rock fracturation (Figure 8). Underneath the low-porosity zone a ~1.0- to 1.5-km-thick zone roughly centered in the subduction channel shows a marked decrease in the vertical velocity gradient and locally a low-velocity zone (Figures 4a and 9). This zone is reasonably well constrained between km ~135–155 at ~12–18 km depth only (Figure 4c), but its location suggests that it may partly correspond to the channel with water-saturated slope debris and eroded upper plate material collected in grabens of the subducting plate.

5.3. Transition to the Seismogenic Zone

[31] Wide-angle and gravity data give information on the structure of the region of transition from aseismic creep to the updip limit of rupture of the M_w = 8.0 Antofagasta 1995 earthquake. The extent of seismic rupture is assumed to be defined by the aftershock sequence recorded during 3 months immediately after the great earthquake with a dense local onshore-offshore seismic network [*Husen et al.*, 1999]. The main shock initiated at ~46 km depth [*Delouis et al.*, 1997] and the rupture extended updip to 18 ± 2 km depth (Figure 10) [*Husen et al.*, 1999]. Aftershock seismicity corresponds well with the position of the plate boundary

constrained by wide-angle data up to ~25 km depth (Figures 4a and 10). The seismic velocity of the bottommost upper plate above the area where the main shock and most aftershocks nucleated is 6.0–6.5 km/s (Figure 4a). This velocity is near the bulk rock velocity for lower oceanic crust, indicating that the lower part of the overriding plate is little fractured here. The gradual fluid depletion with depth in the subduction channel makes fluid pressure along the plate boundary to decrease, increasing in turn the friction between downgoing and overriding plates through its dependence on effective pressure [e.g., *Scholz*, 1998]. The low porosity of the upper plate indicates a coherent framework that can store elastic energy to be released during earthquakes. Aftershock seismicity is more abundant between 45–32 km depth and rapidly decreases updip to a few events between 30–20 km depth and one event at 18 km depth, where the decrease in the velocity gradient along the interplate boundary is best constrained. Thus the downdip transition from stable slip to seismic rupture seems to be gradual and may fundamentally be controlled by declining pore fluid pressure in combination with a decrease in upper plate fracturation with depth and an increase of stress on the thrust fault by the increase in overburden pressure.

5.4. A Tectonic Model of Margin Evolution

[32] The shallow structure of the continental shelf and emerged forearc of northern Chile is extended by landward dipping normal faults [*Armijo and Thiele*, 1990; *Hartley and Jolley*, 1995; *Delouis et al.*, 1998; *Hartley et al.*, 2000]. Extension across the area is probably produced by the lateral loss of support as material is removed by tectonic erosion and the continental margin subsides [*von Huene and Ranero*, 2003]. Mejillones Peninsula is a seaward tilted block bounded to the east by active landward dipping faults [*Delouis et al.*, 1998], comparable to the submerged Antofagasta Ridge and a fault-dismembered ridge to the north [*von Huene and Ranero*, 2003] (Figure 1). The high relief of Mejillones Peninsula, caused by ~2-m.y.-long recent uplift, may be a response to flexural unloading leading to footwall uplift as extension progresses.

[33] Figure 10 shows a tectonic model of the margin resulting from the integration of structural information [*Delouis et al.*, 1998; *von Huene and Ranero*, 2003] with the velocity, density, and porosity models (Figures 4a, 6a, and 8) and the aftershock seismicity. The cross section can be interpreted as showing the temporal evolution of tectonic styles and margin structure as subduction erosion removes material from the front and underside of the overriding plate. Rocks and structures currently near the trench were likely in a situation akin to the structure in the coastal area several m.y. ago and progressive deformation has brought them to their current position and physical state.

[34] The thin front of the margin is highly fragmented by fracturing caused by continuous riffling over subducting plate relief. As debris is carried down in the subduction zone, overpressured fluids are progressively expelled, hydrofracturing the base of the overriding plate. Depth images show that grabens continue deepening in relief under the margin (Figure 9), collecting material eroded by hydrofracturing [*von Huene and Ranero*, 2003]. The markedly higher velocity above the thin subhorizontal detachment indicates that little fluid crosses this boundary and probably collect in the low-velocity zone located below. The detachment is a first-order discontinuity that decouples the deformation style above and below it. Although the detachment surface has been imaged in the seismic reflection data only beneath the middle slope, it probably extends along the top of the low-velocity zone beneath the upper slope and emerged forearc (Figure 10). Above the detachment extensional faulting dominates tectonics, but faulting style and amount of extension changes notably from the subaerial forearc to the middle slope. In the east, forearc extensional tectonics is characterized by large widely spaced landward dipping faults. Across the onshore-offshore transition the number of landward dipping faults seems to increase. Here, the top of the low-velocity zone is located at ~9 km depth, and probably represents the maximum depth of faulting and the base of the area under extension.

[35] The structure of the transition from the continental shelf to the middle slope is not covered by the seismic reflection images, but is constrained by seafloor morphology (Figure 1) and the location of the top of the low-velocity zone. In the upper slope landward dipping faults dismember the upper plate into large blocks and the detachment progressively shallows seaward beneath the seafloor. A change in extensional style and seafloor morphology occurs from the continental shelf to the middle slope where tectonism is dominated by closely spaced seaward dipping faults. Despite this change, the detachment continues to shallow seaward, indicating a continued upper plate extensional thinning. The change from landward to seaward dipping faults could be caused by progressive rotation of landward dipping faults to the angle where they become locked and the initiation of a new seaward dipping set of faults to accommodate the slope steepening due to basal erosion.

6. Conclusions

[36] Modeling of wide-angle seismic data of an onshore-offshore transect and marine gravity data has allowed to determine the structure and physical properties of the north Chile erosive convergent margin in the region of Antofagasta. This information and the tectonic structure obtained from seismic images and multibeam bathymetry have been used to propose a tectonic model. Comparison of the structure with the distribution of aftershocks of the 1995 M_w = 8.0 Antofagasta earthquake gives insights into processes that influence earthquake generation. This work leads to the following conclusions.

[37] 1. The velocity-derived density model shows that the margin is mainly formed by igneous rocks representing a probably pre-Jurassic magmatic arc.

[38] 2. Beneath the lower slope, the basement has low velocity and porosity above critical values. Here the basement is mostly disaggregated, does not show localized large faults, and infiltrated by fluids expelled from compacting underthrusted debris.

[39] 3. Beneath the slope the subduction channel seems to be characterized by a gentle velocity-depth gradient, although not well constrained by wide-angle velocities. Overpressured fluids from the subduction channel may hydrofracture the base of the upper plate.

[40] 4. Fluids escaping from the subduction channel gradually collect within the basement across a low-

velocity body extending from beneath the middle slope to the subaerial forearc. The margin above the low-velocity body is dominated by extensional tectonics. The top of the low-velocity zone forms a gently landward dipping detachment surface where normal faults sole out. Extensional faulting progressively dismembers and thins the upper plate above the detachment from ~9 km thick onshore to ~1 km thick in the middle slope. Thus the continental margin is being thinned by subduction erosion along the base of the plate and by extension across the upper ~9 km.

[41] 5. The transition from creep to the updip limit of the seismogenic zone along the plate boundary roughly coincides with a change of physical properties of the subduction channel and the overriding plate. The creep to stick-slip transition is concurrent with a velocity increase to >6 km/s and a porosity decrease to <5% of the lower part of the continental basement. The decline in fluid content at the plate boundary leads to increased friction and the increase in strength of the overriding plate allows storing of elastic energy. These two parameters may exert a fundamental control in the location of the seismogenic zone.

[42] In summary, the fluids subducted with the slope debris seem to play a fundamental role influencing the long-term tectonic processes of the continental plate as well as the location of the seismogenic zone. Fluids in the subduction channel may be governing basal tectonic erosion and their migration through the upper plate may control the localization of the intrabasement detachment and the locus of extension of the upper plate. When fluids are expelled out of the subduction channel mechanical coupling of the plates increases and large earthquakes may occur.

[43] **Acknowledgments.** The CINCA data were collected during R/V *SONNE* cruise 104 funded by the German Bundesministerium für Bildung und Forschung (BMBF). First author was supported by the EU Program "Improving Human Potential", Access to Research Infrastructure, project: HPRI-CT-1999-00037, during his visit at IFM-GEOMAR to work on this project. The CINCA land wide-angle records were kindly provided by Stefan Lueth from Free University Berlin. We acknowledge Associate Editor, Isabelle Manighetti, and referees Stephan Husen and David Scholl for their insightful reviews, which helped to improve substantially the initial version of the manuscript. Many ideas presented here have benefited from discussion with Roland von Huene. This is contribution 70 of Sonderforschungsbereich 574 and contribution 730 of Géosciences Azur.

References

Armijo, R., and R. Thiele (1990), Active faulting in northern Chile: Ramp stacking and lateral decoupling along a subduction plate boundary?, *Earth Planet. Sci. Lett.*, *98*, 40–61.

Ballance, P. F., D. W. Scholl, T. L. Vallier, A. J. Stevenson, and H. Ryan (1989), Subduction of a late Cretaceous seamount of the Louisville Ridge at the Tonga Trench: A model of normal and accelerated tectonic erosion, *Tectonics*, *8*, 953–962.

Birch, F. (1961), The velocity of compressional waves in rocks to 10 kilobars, part 2, *J. Geophys. Res.*, *66*, 2199–2224.

Carlson, R. L., and C. N. Herrick (1990), Densities and porosities in the oceanic crust and their variations with depth and age, *J. Geophys. Res.*, *95*, 9153–9170.

Christensen, N. I., and W. D. Mooney (1995), Seismic velocity structure and composition of the continental crust: A global view, *J. Geophys. Res.*, *100*, 9761–9788.

Christensen, N. I., and M. H. Salisbury (1975), Structure and constitution of the lower oceanic crust, *Rev. Geophys.*, *13*, 57–86.

Delouis, B., et al. (1997), The *Mw* = 8.0 Antofagasta (northern Chile) earthquake of 30 July 1995: A precursor to the end of the large 1877 gap, *Seismol. Soc. Am. Bull.*, *87*, 427–445.

Delouis, B., H. Philip, L. Dorbath, and A. Cisternas (1998), Recent crustal deformation in the Antofagasta region (northern Chile) and the subduction process, *Geophys. J. Int.*, *132*, 302–338.

Erickson, S. N., and R. D. Jarrard (1998), Velocity-porosity relationships for water-saturated siliciclastic sediments, *J. Geophys. Res.*, *103*, 30,385–30,406.

Fisher, R. L., and R. W. Raitt (1962), Topography and structure of the Peru-Chile trench, *Deep Sea Res.*, *9*, 423–443.

Hamilton, E. L. (1978), Sound velocity-density relations in seafloor sediments and rocks, *J. Acoust. Soc. Am.*, *63*, 366–377.

Hartley, A. J., and G. Chong (2002), Late Pliocene age for the Atacama Desert: Implications for the desertification of western South America, *Geology*, *30*, 43–46.

Hartley, A. J., and E. J. Jolley (1995), Tectonic implications of Late Cenozoic sedimentation from the Coastal Cordillera of northern Chile (22–24°S), *J. Geol. Soc. London*, *152*, 51–63.

Hartley, A. J., G. May, G. Chong, P. Turner, S. J. Kape, and E. J. Jolley (2000), Development of a continental forearc: A Cenozoic example from the central Andes, northern Chile, *Geology*, *28*, 331–334.

Hashin, Z., and S. Shtrikman (1963), A variational approach to the elastic behavior of multiphase materials, *J. Mech. Phys. Solids*, *11*, 127–140.

Hayes, D. E. (1966), A geophysical investigation of the Peru-Chile Trench, *Geology*, *4*, 309–351.

Hinz, K., et al. (1995), Geowissenschaftliche Untersuchungen off- und onshore Zentralanden an der aktiven sudostpazifischen Subduktionszone – CINCA, *Rep. SONNE-Fahrt SO-104/1, 22.07.–24.08.1995*, Bundesanst. für Geowiss. und Rohstoffe, Hannover, Germany.

Husen, S., and E. Kissling (2001), Postseismic fluid flow after the large subduction earthquake of Antofagasta, Chile, *Geology*, *29*, 847–850.

Husen, S., E. Kissling, E. Flueh, and G. Asch (1999), Accurate hypocenter determination in the seismogenic zone of the subducting Nazca plate in north Chile using a combined on-/offshore network, *Geophys. J. Int.*, *138*, 687–701.

Husen, S., E. Kissling, and E. R. Flueh (2000), Local earthquake tomography of shallow subduction in north Chile: A combined onshore and offshore study, *J. Geophys. Res.*, *105*, 28,183–28,198.

Hussong, D. M., and S. Uyeda (1981), Tectonic processes and the history of the Mariana Arc: A synthesis of the results of DSDP Leg 60, *Initial Rep. Deep Sea Drill. Proj.*, *60*, 909–929.

Korenaga, J., W. S. Holbrook, G. M. Kent, P. B. Kelemen, R. S. Detrick, H.-C. Larsen, J. R. Hopper, and T. Dahl-Jensen (2000), Crustal structure of the southeast Greenland margin from joint refraction and reflection seismic tomography, *J. Geophys. Res.*, *105*, 21,591–21,614.

Korenaga, J., W. S. Holbrook, R. S. Detrick, and P. B. Kelemen (2001), Gravity anomalies and crustal structure at the southeast Greenland margin, *J. Geophys. Res.*, *106*, 8853–8870.

Kulm, L. D., W. J. Schweller, and A. Masias (1977), A preliminary analysis of the subduction process along the Andean continental margin near 6° to 45°S, in *Island Arcs, Deep-Sea Trenches, and Back-Arc Basins*, *Maurice Ewing Ser.*, vol. 1, edited by M. Talwani and W. C. Pitman III, pp. 285–301, AGU, Washington, D. C.

Mavko, G., T. Mukerji, and J. Dvorkin (1998), *The Rock Physics Handbook*, 329 pp., Cambridge Univ. Press, New York.

Miller, H. (1970), Das Problem des hypothetischen "Pazifischen Kontinentes" gesehen von der chilenischen Pazifikkuste, *Geol. Rundsch.*, *59*, 927–938.

Mukerji, T., J. Berryman, G. Mavko, and P. Berge (1995), Differential effective medium modelling of rock elastic moduli with critical porosity constraints, *Geophys. Res. Lett.*, *22*, 555–558.

Nur, A., D. Marion, and H. Yin (1991), Wave velocities in sediments, in *Shear Waves in Marine Sediments*, edited by J. M. Hoven, M. D. Richardson, and R. D. Stoll, pp. 131–140, Springer, New York.

Nur, A., G. Mavko, J. Dvorkin, and D. Galmudi (1998), Critical porosity: A key relating physical properties to porosity in rocks, *Leading Edge*, *17*, 357–362.

Pardo Casas, F., and P. Molnar (1987), Relative motion of the Nazca (Farallon) and South American plates since Late Cretaceous time, *Tectonics*, *6*, 233–248.

Parker, R. L. (1972), The rapid calculation of potential anomalies, *Geophys. J. R. Astron. Soc.*, *31*, 447–455.

Patzwald, R., J. Mechie, A. Schulze, and P. Giese (1999), Two-dimensional velocity models of the Nazca plate subduction zone between 19.5°S and 25°S from wide-angle seismic measurements during the CINCA95 project, *J. Geophys. Res.*, *104*, 7293–7317.

Pelletier, B., and J. Dupont (1990), Effects de la subduction de la ride de Louisville sur l'arc des Tonga-Kermadec, *Oceanol. Acta*, *10*, 57–76.

Ranero, C. R., and V. Sallarès (2004), Geophysical evidence for alteration of the crust and mantle of the Nazca Plate during bending at the north Chile trench, *Geology*, *32*, 549–552.

Ranero, C. R., and R. von Huene (2000), Subduction erosion along the Middle America convergent margin, *Nature*, *404*, 748–752.

Ranero, C. R., R. von Huene, E. Flueh, M. Duarte, D. Baca, and K. McIntosh (2000), A cross-section of the convergent Pacific margin of Nicaragua, *Tectonics*, *19*, 335–357.

Ranero, C. R., J. Phipps Morgan, K. McIntosh, and C. Reichert (2003), Bending, faulting, and mantle serpentinization at the Middle America trench, *Nature*, *425*, 367–373.

Raymer, L. L., E. R. Hunt, and J. S. Gardner (1980), An improved sonic transit time-to-porosity transform, *Trans. SPWLA Annu. Logging Symp.*, *21*, P1–P13.

Rutland, R. W. R. (1971), Andean orogeny and ocean floor spreading, *Nature*, *233*, 252–255.

Sallarès, V., J. J. Dañobeitia, and E. Flueh (2001), Lithospheric structure of the Costa Rican Isthmus: Effects of subduction zone magmatism on an oceanic plateau, *J. Geophys. Res.*, *106*, 621–643.

Sallarès, V., P. Charvis, E. R. Flueh, and J. Bialas (2003), Seismic structure of Malpelo and Cocos volcanic ridges and implications for hotspot-ridge interaction, *J. Geophys. Res.*, *108*(B12), 2564, doi:10.1029/2003JB002431.

Sallarès, V., P. Charvis, E. R. Flueh, J. Bialas, and SALIERI Working Group (2005), Seismic structure of Carnegie Ridge and the nature of the Galapagos hotspot, *Geophys. J. Int.*, in press.

Scholz, C. H. (1998), Earthquakes and friction laws, *Nature*, *391*, 37–42.

Tarantola, A. (1987), *Inverse Problem Theory: Methods for Data Fitting and Model Parameter Estimation*, 613 pp., Elsevier, New York.

Toomey, D. R., and G. R. Foulger (1989), Tomographic inversion of local earthquake data from the Hengill-Grensdalur central volcano complex, Iceland, *J. Geophys. Res.*, *94*, 17,497–17,510.

van Avendonk, H. J. A., A. J. Harding, and J. A. Orcutt (1998), A two-dimensional tomographic study of the Clipperton transform fault, *J. Geophys. Res.*, *103*, 17,885–17,899.

Vannucchi, P., C. R. Ranero, S. Galeotti, S. M. Straub, D. W. Scholl, and K. McDougall-Ried (2003), Fast rates of subduction erosion along the Costa Rica Pacific margin: Implications for nonsteady rates of crustal recycling at subduction zones, *J. Geophys. Res.*, *108*(B11), 2511, doi:10.1029/2002JB002207.

Vannucchi, P., S. Galeotti, P. Clift, C. R. Ranero, and R. von Huene (2004), Long term subduction erosion along the Middle America Trench offshore Guatemala, *Geology*, *32*, 617–620.

von Huene, R., and S. Lallemand (1990), Tectonic erosion along the Japan and Peru convergent margins, *Geol. Soc. Am. Bull.*, *102*, 704–720.

von Huene, R., and C. R. Ranero (2003), Subduction erosion and basal friction along the sediment starved convergent margin off Antofagasta, Chile, *J. Geophys. Res.*, *108*(B2), 2079, doi:10.1029/2001JB001569.

von Huene, R., and D. W. Scholl (1991), Observations at convergent margins concerning sediment subduction, subduction erosion, and the growth of continental crust, *Rev. Geophys.*, *29*, 279–316.

von Huene, R., C. R. Ranero, W. Weinrebe, and K. Hinz (2000), Quaternary convergent margin tectonics of Costa Rica, segmentation of the Cocos Plate, and Central American volcanism, *Tectonics*, *19*, 314–334.

White, R. S., D. McKenzie, and R. K. O'Nions (1992), Oceanic crustal thickness from seismic measurements and rare earth element inversions, *J. Geophys. Res.*, *97*, 19,683–19,715.

Wyllie, M. R. J., A. R. Gregory, and L. W. Gardner (1956), Elastic wave velocities in heterogeneous and porous media, *Geophysics*, *21*, 41–70.

Yañez, G. A., C. R. Ranero, R. von Huene, and J. Diaz (2001), Magnetic anomaly interpretation across the southern central Andes (32°–34°S): The role of the Juan Fernandez Ridge in the late Tertiary evolution of the margin, *J. Geophys. Res.*, *106*, 6325–6345.

C. R. Ranero, ICREA, Institut de Ciències del Mar, CMIMA-CSIC, Passeig Marítim de la Barceloneta 37-49, E-08003 Barcelona, Spain. (cranero@icm.csic.es)

V. Sallarès, Unitat de Tecnologia Marina, CMIMA–CSIC, Passeig Marítim de la Barceloneta 37-49, E-08003 Barcelona, Spain. (vsallares@utm.csic.es)

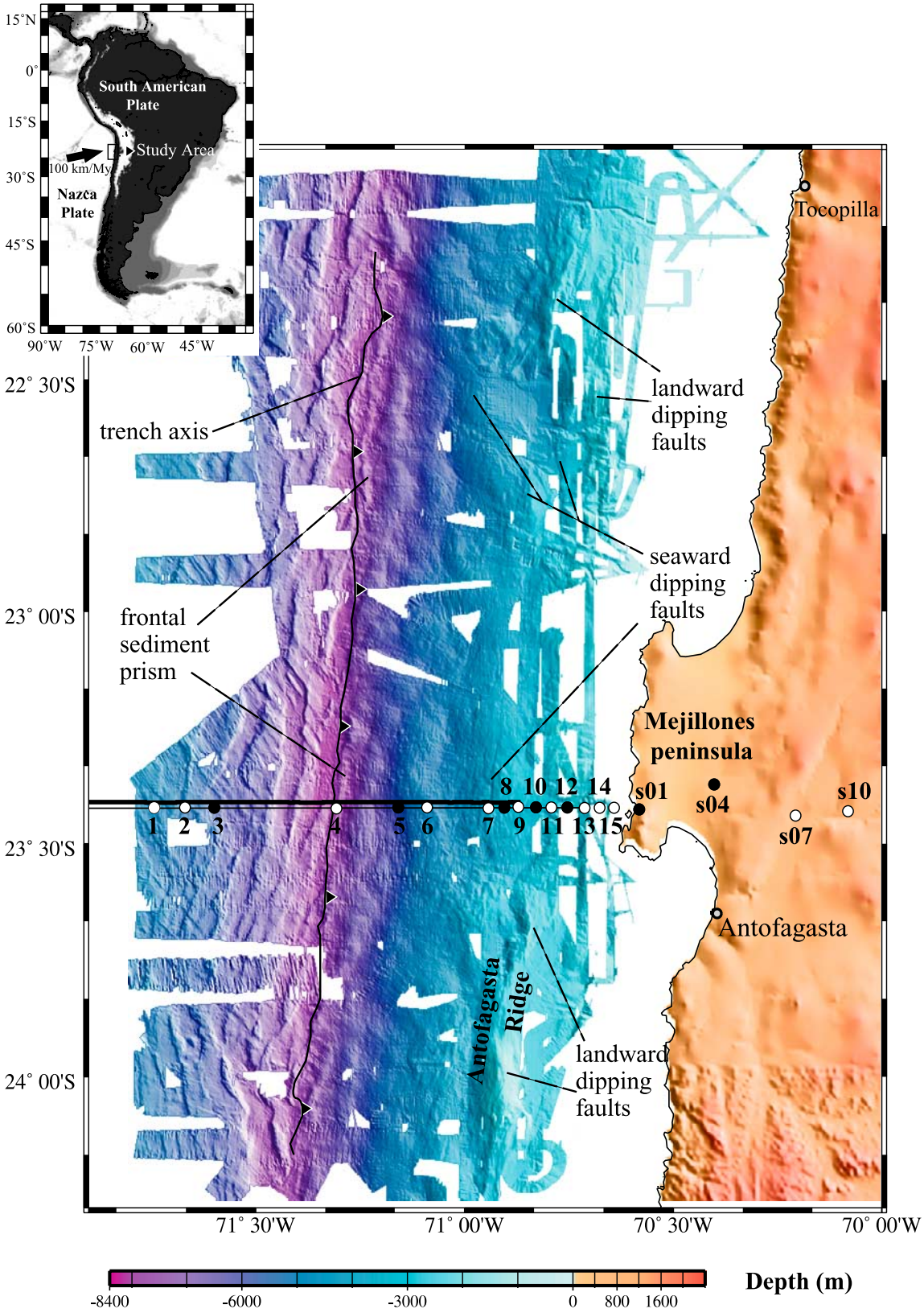

Figure 1. Shaded relief map of the multibeam bathymetry offshore of the Antofagasta sector of northern Chile. Inset shows a regional location map. The arrow displays the convergence direction of the Nazca plate with respect to the South American plate. Thick line is the track of the seismic reflection profile, and thinner line indicates the extent of wide-angle shooting and gravity data acquired offshore Mejillones peninsula. Circles indicate ocean bottom hydrophones and land stations used in the seismic modeling. The record sections of the instruments indicated by solid circles are shown in Figure 2.

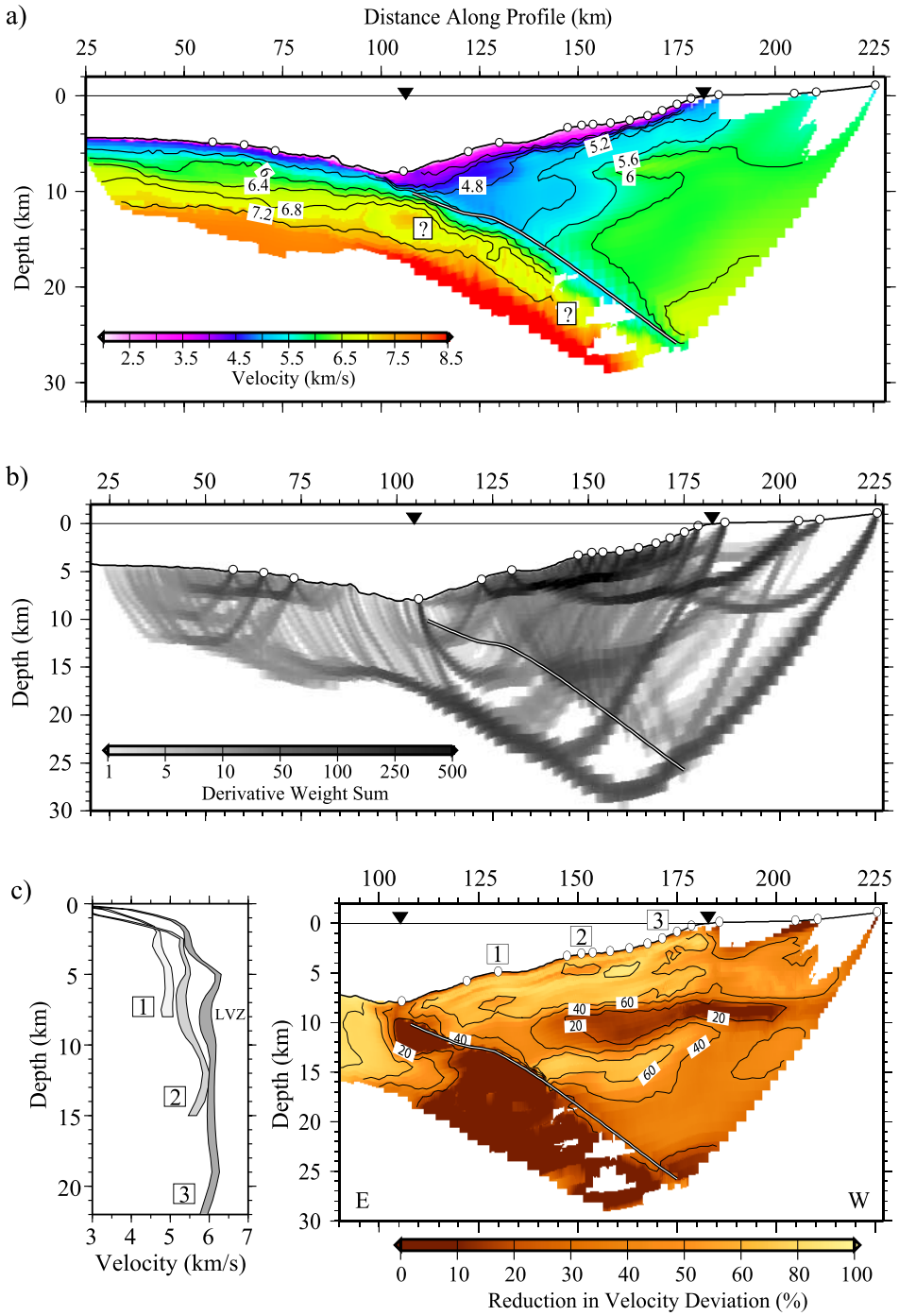

Figure 4. (a) Final velocity model with isovelocity contours. Thick white line shows location of the interplate boundary derived from inversion of P_iP reflection travel times. White circles indicate OBH and land stations locations. Arrows show the location of the trench and the coastline. (b) Derivative weight sum (DWS). (c) (right) Improvement of mean deviation of all the Monte Carlo realizations with respect to the reference velocity models. Numbers indicate location of the 1-D velocity profiles shown in Figure 4c (left). (left) The 1-D velocity profiles. The shaded area shows the horizontally averaged velocity deviation estimated from the Monte Carlo analysis.